International Journal of Fatigue 183 (2024) 108267

Contents lists available at ScienceDirect

International Journal of Fatigue

journal homepage: www.elsevier.com/locate/ijfatigue

Retardation mechanisms and modeling of fatigue crack growth of a high-strength steel after single overload

Youlin Li [a], Lu Ke [a,b,*], Chuanxi Li [a], Peng Feng [b], Zheng Feng [a], Mingdong Qiu [a]

[a] State Key Laboratory of Featured Metal Materials and Life-cycle Safety for Composite Structures, School of Civil Engineering and Architecture, Guangxi University, Nanning 530004, China

[b] Department of Civil Engineering, Tsinghua University, Beijing 100084, China

ARTICLE INFO

Keywords:
Fatigue crack growth
Retardation behavior
Steel
Single overload
Plastic zone

ABSTRACT

This study investigated the retardation mechanisms and modeling methodology for the fatigue crack growth (FCG) of a high-strength Q500qE steel after a single overload. Different stress ratios (R = 0.1, 0.3, and 0.5) and overload ratios (OLR = 1.5, 2.0, and 2.5) were considered as key parameters. The digital image correlation (DIC) testing technique was used to capture the deformation at the crack tip during the tests. The crack closure response in the crack wake region was investigated using a virtual extensometer. The results show that, under an identical stress ratio, the fatigue life was increased as the OLR increased. The FCG was completely arrested when OLR reached 2.5 when $R \geq 0.3$. Under an identical stress ratio, the residual strain before the crack tip and the residual deformation in the crack wake region increased with the rise of the overload ratio after a single overload. It's found that the FCG was retarded or completely arrested due to the constraint of the crack tip plastic zone caused by single overload. Finally, a modified Wheeler model was proposed to predict the FCG rate based on the measured plastic zone size at the crack tip, and the predicted results agree well with the experimental findings.

1. Introduction

High-strength steel, such as Q500qE, is favored for constructing steel bridges due to its high tensile strength and fracture toughness. Fatigue problem is a key factor affecting the long-term performance of steel bridges [1–3], which may be attributed to the increasing traffic loads [4–7]. In particular, bridge steel structures often suffer from variable amplitude fatigue loading under traffic loads. Therefore, it's of great significance to provide theoretical guidance for designing, evaluating, and maintaining high-strength steel bridges by through knowledge of the fatigue crack growth (FCG) behavior under variable amplitude loading.

Single overload is a common variable-amplitude fatigue load during the service of steel bridges. Generally, the FCG response of steel material after a single overload can be divided into five stages [8], including the stable growth stage before overload, the instantaneous acceleration stage, the delayed retardation stage, the retardation stage, and the stable growth stage after retardation completion, as shown in Fig. 1. However, previous studies [9,10] have shown that some materials do not fully comply with the five-stage retardation response. For example, Correia et al. [11] found that cast iron materials have no instantaneous acceleration stage after a single overload while showing a gradual decrease in fatigue crack growth rate (FCGR) after applying overload. Wang et al. [12] obtained similar experimental results in the single overload test on aluminum alloy 7050-T7451. In addition, Ren et al. [13] found that superalloy 625 did not acquire FCGR data for the delayed retardation stage after a single overload. Similarly, Albedah et al. [14] did not acquire FCGR data for the delayed retardation stage in the testing for aluminum alloys 2024-T3 and 7075-T6. It can be seen that different metal materials may behave differently in FCG after single overload. Therefore, it is necessary to carry out FCG tests incorporating a single overload to unveil the FCG mechanisms of high-strength steel.

Up to now, researchers have conducted a series of theoretical and experimental studies on the FCG behavior after a single overload and proposed various retardation mechanisms to explain the FCG retardation behavior. For example, residual stress theory [15–18], crack closure theory [19–21], crack deflection theory [22,23], crack tip blunting theory [24], and strain hardening theory [25]. The commonly used theories include residual stress theory (crack tip plasticity theory), crack closure theory, and so on. He et al. [26] found that the size of the compressive residual stress field ahead of the crack tip increased with

* Corresponding author at: School of Civil Engineering and Architecture, Guangxi University, Nanning, Guangxi 530004, China.
E-mail address: kelu@gxu.edu.cn (L. Ke).

https://doi.org/10.1016/j.ijfatigue.2024.108267
Received 21 November 2023; Received in revised form 31 January 2024; Accepted 5 March 2024
Available online 7 March 2024

Nomenclature

FCG	fatigue crack growth
FCGR	fatigue crack growth rate
TMCP	thermomechanical control process
CT	compact tension
DIC	digital image correlation
COD	crack opening displacement
EDM	electro discharge machining
R	stress ratio
OLR	overload ratio
da/dN	fatigue crack growth rate
K	stress intensity factor
ΔK	stress intensity factor amplitude
a	crack length
N	number of load cycles
E	elastic modulus
σ_{ys}	yield strength
P_{OL}	single overload force
P_{max}	upper limit of fatigue load
P_{min}	lower limit of fatigue load
ΔP	load range
W	width of CT specimens
B	thickness of CT specimens
R^2	coefficient of determination
a_{OL}	crack length when applying single overload
$(da/dN)_{be,max}$	maximum fatigue crack growth rate before applying the overload
$(da/dN)_{min}$	minimum fatigue crack growth rate after applying single overload
η	retardation coefficient
ε_{yy}	strain in Y direction
ε_{res}	residual strain
r_p	plastic zone size
α	plastic factor of the retardation stage
β	plastic factor of the delayed retardation stage
ϕ_R	retardation parameter
$r_{p,i}$	plastic zone size at the current crack length in retardation stage
$r_{p,OL}$	plastic size applied the overload
m_{org}	dimensionless shape parameter
K_i	stress intensity factor at current crack length
K_{OL}	stress intensity factor applied overload
K_r	maximum stress intensity factor at the retardation stage
a_r	crack length of the retardation stage
ϕ_D	delayed retardation parameter
$r_{d,OL}$	plastic zone size of delayed retardation stage
$r_{d,i}$	plastic zone size at current crack length in delayed retardation stage
m_{mod}	modified shape parameter
a_d	crack length of the delayed retardation stage
K_d	maximum stress intensity factor at delayed retardation stage
$\phi_{R,modified}$	modified retardation parameter
$a_{min(da/dN)}$	crack length corresponding to the minimum fatigue crack growth rate after a single overload

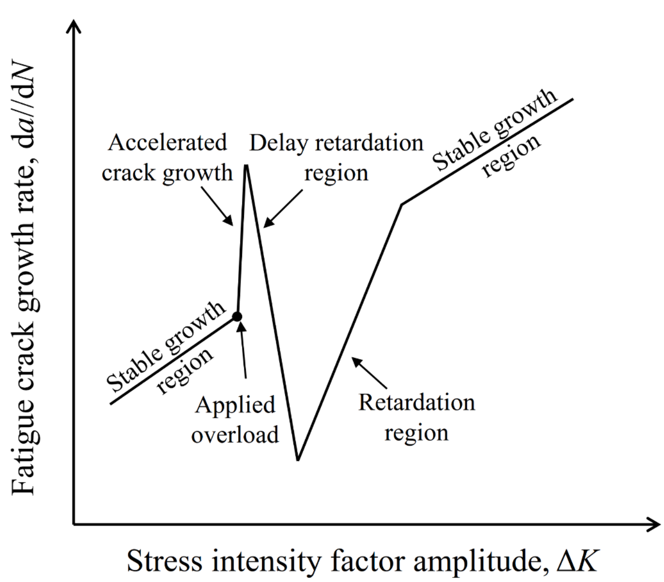

Fig. 1. Fatigue crack growth stage incorporating a single overload [8].

the overload ratio, and the larger the compressive residual stress value, the stronger the retardation effect. Francisco et al. [27] found that plastic deformation at the crack tip was the primary damage mechanism of Grade 2 titanium after a single overload. Cai et al. [28] found that the retardation degree of crack growth in 2024-T3, 7075-T6, and 6061-T6 aluminum alloys after applying a single overload was mainly controlled by the residual stress and plastic deformation ahead of the crack tip. Chen et al. [29] found that the compressive residual stress was leading in retarding FCG after a single overload in AZ31, while crack closure was secondary. In addition, Geng et al. [30] experimentally studied the FCG behavior of steel AH32 after a single overload and found that new residual plastic deformation was formed at the tensile overload position, and the larger the overload ratio, the greater the contribution of plastic-induced crack closure to the retardation effect. Su et al. [31] carried out the fatigue short crack growth tests of steel EH36 and found that the reduction in FCGR in the retardation stage was mainly attributed to crack closure and residual strain effects. In conclusion, the retardation mechanisms of different materials after a single overload are not wholly consistent and are usually intertwined by various retardation mechanisms. Therefore, it is necessary to conduct further research to reveal the FCG retardation mechanisms of high-strength steel and to establish a more general model.

A series of mathematical models were proposed for predicting the FCGR accurately after applying a single overload. The Wheeler model was widely used due to its simple form and ease of calculation [32]. However, this model can only calculate the FCGR in the retardation stage but not calculate the FCGR in the delayed retardation and the instantaneous acceleration stages. Therefore, Yuen and Taheri [8] introduced a delayed retardation parameter into the original Wheeler model to modify it. The results showed that the modified model could reasonably predict the FCGR of steel 350 WT in the entire retardation stage (including the delayed retardation stage). In addition, the modified model has been effectively verified on various materials since its proposal [33,34]. With the improvement of computational methods and measurement techniques, researchers have continuously modified the original Wheeler model, and a model that can consider both plastic zone and crack closure effects has been established. For example, Jiang et al. [35] established a complex FCGR prediction model that did not contain any dimensionless retardation parameters and comprehensively considered the effects of crack closure, plastic zone, and the Bauschinger effect after a single overload. Lu et al. [36] introduced the Alpha model that characterized the degree of contribution of the crack closure effect to the overload effect and established the Wheeler-Alpha model. This

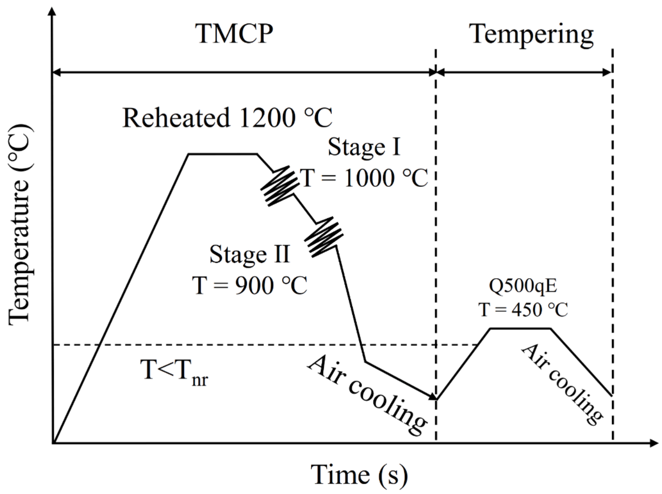

Fig. 2. Schematic of a Q500qE steel annealing heat treatment.

model had a high degree of agreement between the predicted and the experimental results for steel QSTE340TM, steel DP780, and 6082-T6 aluminum alloy. However, there is little research on the FCG retardation model of Q500qE steel applying a single overload in the published literature. Therefore, it has great significance for designing fatigue performance and evaluating the fatigue life of Q500qE steel to propose an accurate FCGR prediction retardation model.

In this study, the retardation mechanisms for the FCG of a high-strength Q500qE steel after a single overload was experimentally investigated. The effects of different stress ratios ($R = 0.1$, 0.3, and 0.5) and overload ratios (OLR = 1.5, 2.0, and 2.5) were carefully examined. The plastic zone size at the crack tip was measured using digital image correlation (DIC) technique, and the distribution of the strain field ahead of the crack tip was clarified. The crack opening and closure behavior in the crack wake region was analyzed using the virtual extensometer technique. The FCG retardation mechanisms after a single overload were revealed. Finally, a modified Wheeler model based on the experimental plastic zone size was proposed to predict the FCGR in the whole retardation stages. The outcomes of this study may shed some more light on the unveiling of the retardation behavior of FCG of high-strength steel and therefore advance the fatigue life prediction of high-strength steel structures under complex fatigue loading.

2. Experimental program

2.1. Material and specimen preparation

The material used in the present investigation was a Q500qE high-strength bridge steel with a thickness of 33 mm. In addition, Q500qE steel was subject to a tempering heat treatment based on a conventional thermomechanical control process (TMCP), as shown in Fig. 2. The chemical composition of the Q500qE steel is shown in Table 1.

The ferrite and bainite exhibited bright and dark colors after being corroded by nitric acid alcohol solution under optical microscope, respectively, as shown in Fig. 3. The average equivalent grain size d can be obtained according to the equation as $d = 2(S/\pi)^{1/2}$, where S is the area of grains [4,37], which was calculated by an image processing software Image-Pro Plus. The results show that the average equivalent grain size of bainite was 2.96 μm and standard deviation was 0.02.

The static tensile tests of Q500qE steel were conducted at room temperature, and two replicate tests were performed. The static tensile specimens were machined into a dog-bone shape with the length parallel to the rolling direction of the steel plate according to ASTM E8/E8M [38], and tensile tests were carried out on a universal material testing machine at a tensile rate of 3 mm/min. Fig. 4 shows the dimension and engineering stress-strain relationship of tensile specimens, respectively. It can be seen that the Q500qE steel showed a significant increase in strain after yielding, while the stress increased slightly, indicating that

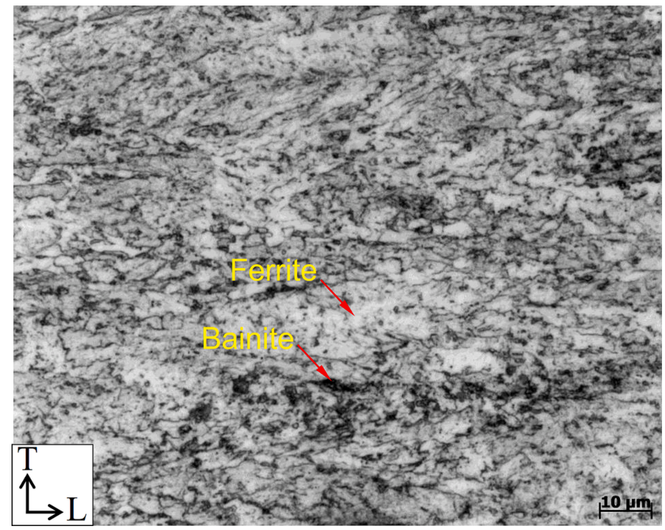

Fig. 3. Microstructure of Q500qE steel after magnifying 1000X. L and T respectively represent the longitudinal and transverse direction of hot rolling.

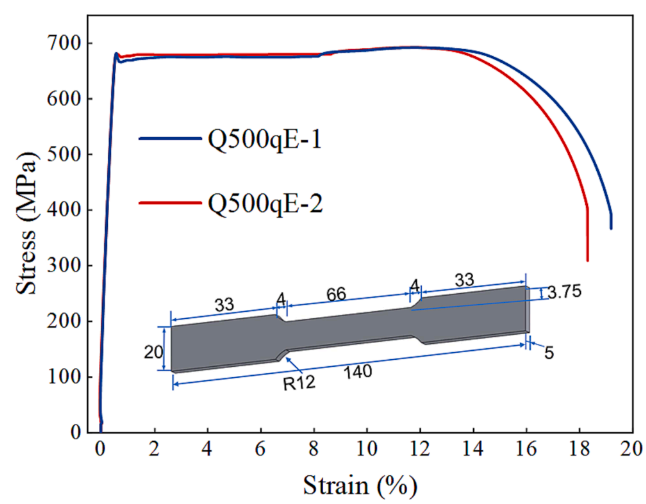

Fig. 4. Engineering stress–strain relationship for Q500qE steel.

Table 2
The tensile properties of Q500qE steel at room temperature.

Steel	E (GPa)	σ_{ys} (MPa)	σ_U (MPa)	δ (%)
Q500qE	205.6	675.8	692.2	18.4

Table 1
Chemical composition of Q500qE steel provided by the material supplier (% weight).

Steel	C	Si	Mn	P	S	Cr	Ni	Nb	Ti
Q500qE	0.057	0.223	1.493	0.010	0.002	0.280	0.206	0.046	0.012

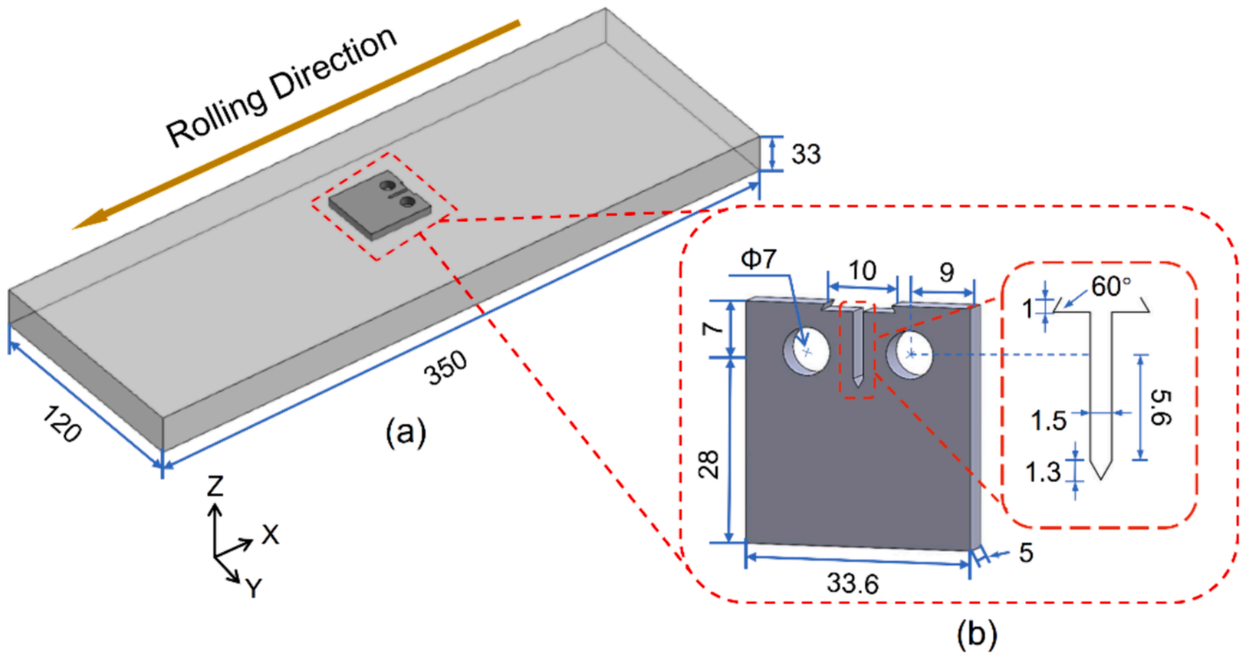

Fig. 5. Geometry and dimensions of the base metal and CT specimens for Q500qE steel: (a) base metal, (b) CT specimens (units in mm).

Table 3
Load conditions of single overload tests.

Specimen number	Stress ratio R	P_{max} (kN)	P_{min} (kN)	Overload Ratio OLR	P_{OL} (kN)
R0.1	0.1	4.00	0.40	–	–
R0.1E1.5	0.1	4.00	0.40	1.5	6.00
R0.1E2.0	0.1	4.00	0.40	2.0	8.00
R0.1E2.5	0.1	4.00	0.40	2.5	10.00
R0.3E1.5	0.3	5.14	1.54	1.5	7.71
R0.3E2.0	0.3	5.14	1.54	2.0	10.28
R0.3E2.5	0.3	5.14	1.54	2.5	12.85
R0.5E1.5	0.5	7.20	3.60	1.5	10.80
R0.5E2.0	0.5	7.20	3.60	2.0	14.40
R0.5E2.5	0.5	7.20	3.60	2.5	18.00

the Q500qE steel exhibited low hardening capacity. The tensile properties of Q500qE steel were listed in Table 2.

Fig. 5 illustrates the geometry of the base metal and fatigue specimens for Q500qE steel. According to the ASTM E647 [39], the FCG tests were carried out using compact tensile (CT) specimens, which were machined by an electro discharge machining (EDM) process. In addition, the notch direction (crack growth direction) of the CT specimen was consistent with the rolling direction of the steel plate.

2.2. Test methodologies

2.2.1. Fatigue crack growth (FCG) tests

The FCG tests were conducted via an Instron 8801 electro-hydraulic servo testing machine. Prior to the crack growth tests, all CT specimens were pre-cracked with a crack length of 1.4 mm – 1.5 mm. Three sets of FCG tests were performed with different stress ratios $R = 0.1, 0.3, 0.5$, and single overload ratios OLR $= 1.5, 2.0, 2.5$. The detailed loading conditions are shown in Table 3, where the overload ratio is defined as the ratio of the single overload force P_{OL} to the upper limit of fatigue load P_{max} of the constant amplitude cyclic loading. Moreover, the specimen labels were denoted by RXEY, where RX and EY represented the stress and overload ratios, respectively. For instance, R0.1E1.5 indicates the specimen tested with a stress ratio of 0.1 and an overload ratio of 1.5.

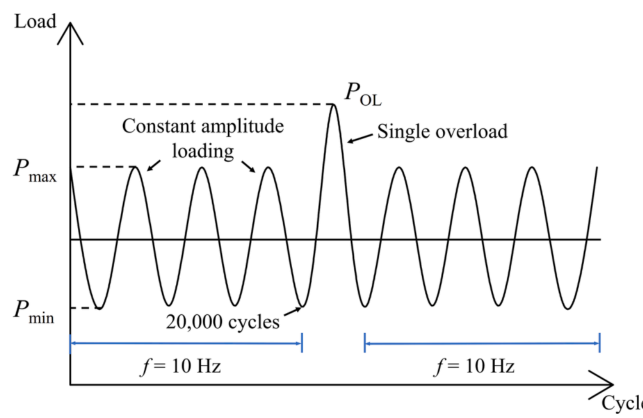

Fig. 6. Schematic of the load spectrum of single overload tests.

The schematic loading spectrum of the single overload test is shown in Fig. 6. The frequency f of the constant amplitude cyclic loading was in a 10 Hz sine waveform. After 20,000 constant amplitude cyclic loading (the FCG was in a stable growth stage), an overload cycle was applied to the CT specimen starting from lower limit of fatigue load P_{min}. Then, the loading frequency was restored to the constant amplitude cyclic loading stage, and the test was continued until the crack length reached 15 mm – 18 mm, and the test was stopped.

A crack opening displacement (COD) gauge was adopted to record the opening displacement of CT specimens during the tests. Then, the crack lengths at the corresponding number of loading cycles were calculated using the opening displacement data according to the compliance method recommended by ASTM E647 [39]. Further, the stress intensity factor (SIF) amplitude was calculated by Eq. (1).

$$\Delta K = \frac{\Delta P}{B\sqrt{W}} \frac{(2+n)}{(1-n)^{3/2}} \left(0.886 + 4.64n - 13.32n^2 + 14.72n^3 - 5.6n^4\right) \tag{1}$$

where $\Delta P = P_{max} - P_{min}$, $n = a/W$. B and W are the thickness and width of the CT specimens, respectively.

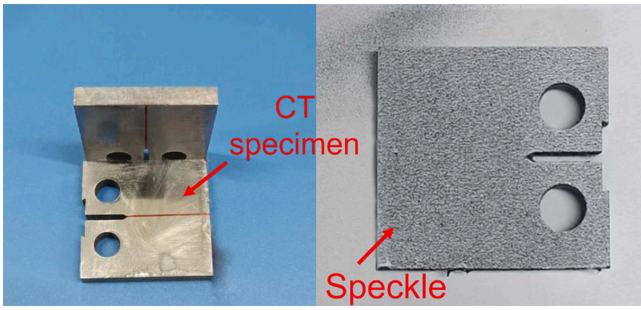

Fig. 7. Speckle production for CT specimens.

2.2.2. Digital image correlation (DIC) measurements

Digital image correlation (DIC) technique plays an important role in testing the surface deformation of materials and components. The deformation field at the crack tip during FCG was measured using the ARAMIS system of the German GOM company in the current study. Prior to conducting the DIC measurement, the surface of the CT specimen should be sprayed with a qualified speckle, as shown in Fig. 7. The GOM correlated 2020 commercialized software was used to identify feature points on the surface. Then, the displacements were obtained by comparing the positions of feature points in the two images before and after deformation. Finally, the strain information of each feature point based on the algorithm embedded in the software was acquired.

The experimental configuration of FCG and DIC tests are shown in Fig. 8. The DIC measurement system provided 4096×3068 pixels digital images via a set of high magnification camera lenses covering an area of

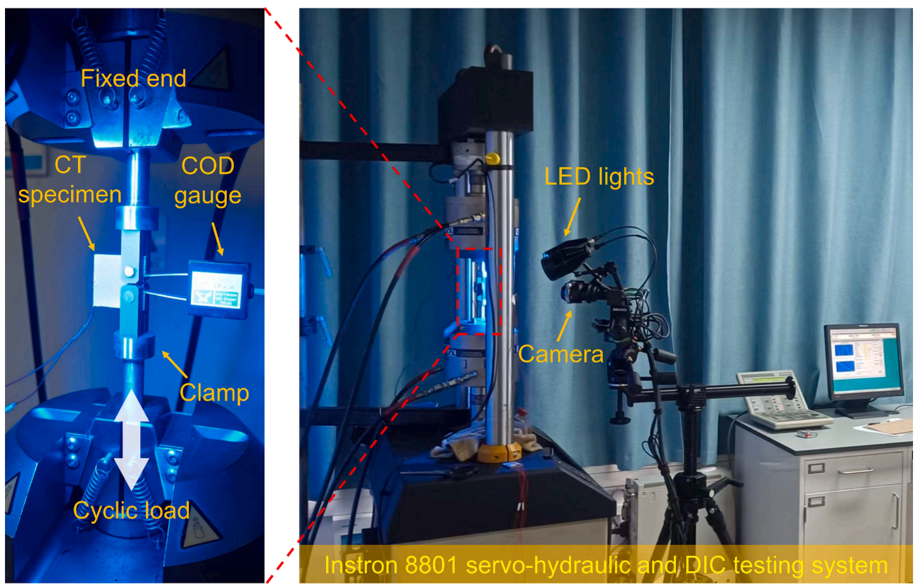

Fig. 8. Fatigue crack growth and DIC tests setup.

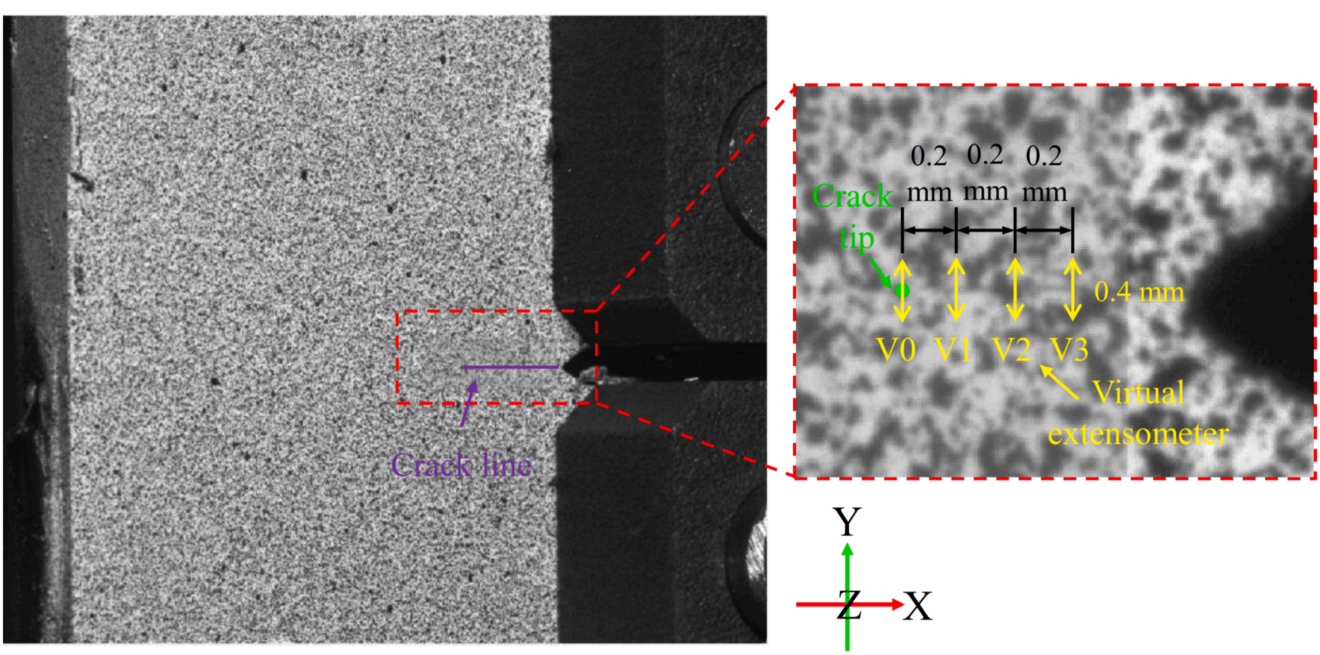

Fig. 9. Virtual extensometer arrangement behind crack tip.

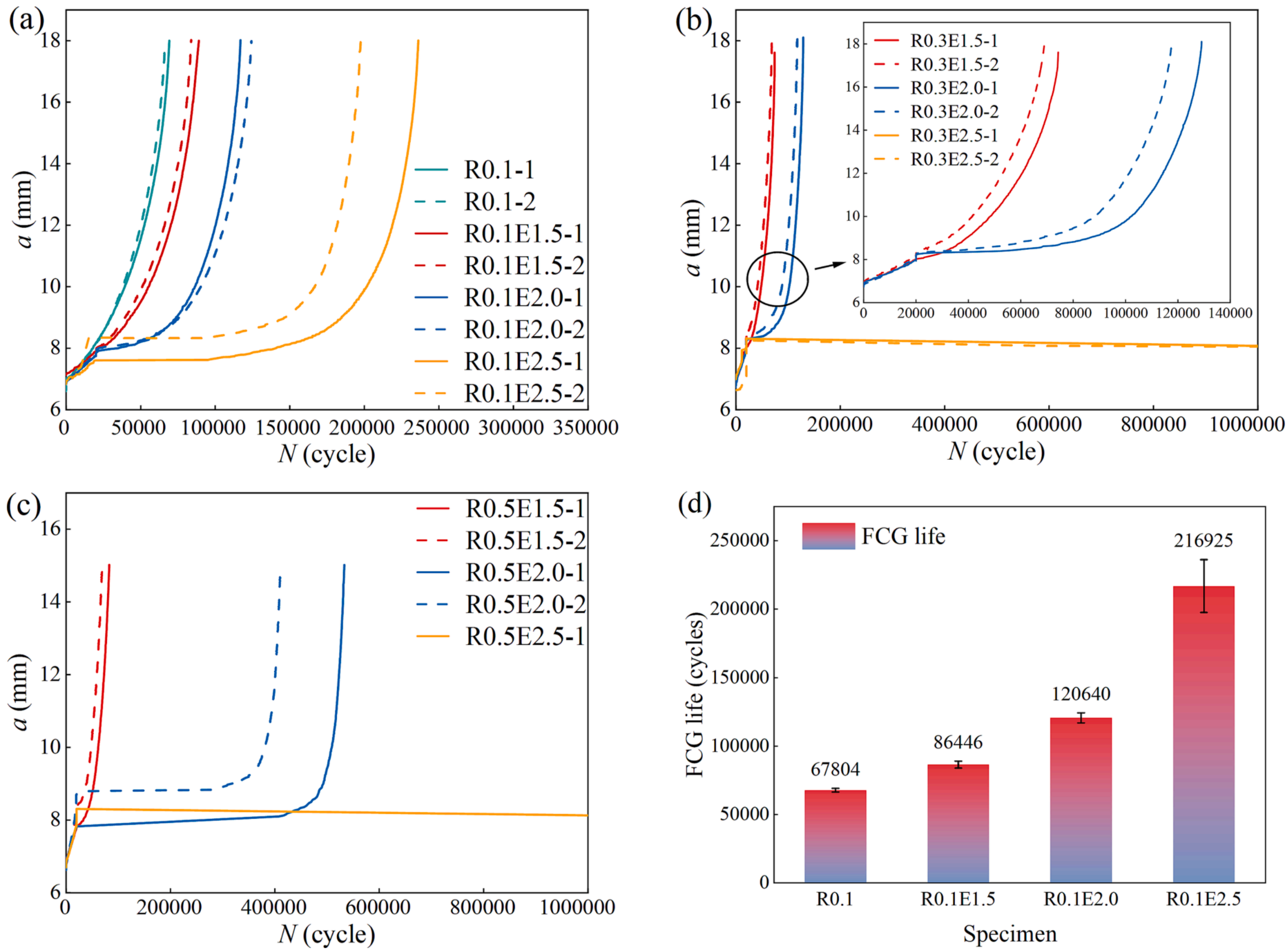

Fig. 10. FCG lives: (a) *a-N* curves for $R = 0.1$; (b) *a-N* curves for $R = 0.3$; (c) *a-N* curves for $R = 0.5$; (d) comparison of fatigue lives.

25 mm × 18 mm on the interested zone. The acquisition frequency for DIC measurements was set to 20 Hz, and the corresponding fatigue loading frequency was set to 0.5 Hz.

2.2.3. Virtual extensometer technology

The crack opening and closure behavior behind the crack tip was examined by a virtual extensometer technology, and it was calculated from the digital images obtained by a DIC measurement [40,41]. For this purpose, four virtual extensometers with a gauge length of 0.4 mm were arranged at 0.2 mm intervals starting at the crack tip along the crack propagation path, as shown in Fig. 9. These virtual extensometers were denoted as V0, V1, V2, and V3, respectively. The digital image corresponding to the minimum load P_{min} during a single overload was taken as the reference image to calculate the extension of each virtual extensometer; thereby the force and displacement relationships at the four virtual extensometers can be obtained.

3. Experimental results and discussion

3.1. Fatigue crack growth

3.1.1. A vs. N curves

The FCG life (*a-N*) curves for all CT specimens are shown in Fig. 10(a – c). The Fig. 10 (d) shows that the average FCG life were increased by 27.49 %, 77.92 % and 219.93 %, corresponding to R0.1E1.5, R0.1E2.0 and R0.1E2.5, respectively, compared to R0.1. It indicates that the fatigue lives of cracked high-strength steel can be effectively enhanced by single overloading. Therefore, the higher the overload ratio, the higher the number of load cycles under the identical stress ratios, indicating that a high overload ratio has an outstanding contribution to the extension of the service life of the material. The opposite result was obtained, i.e., the FCG life increased with the stress ratio under the

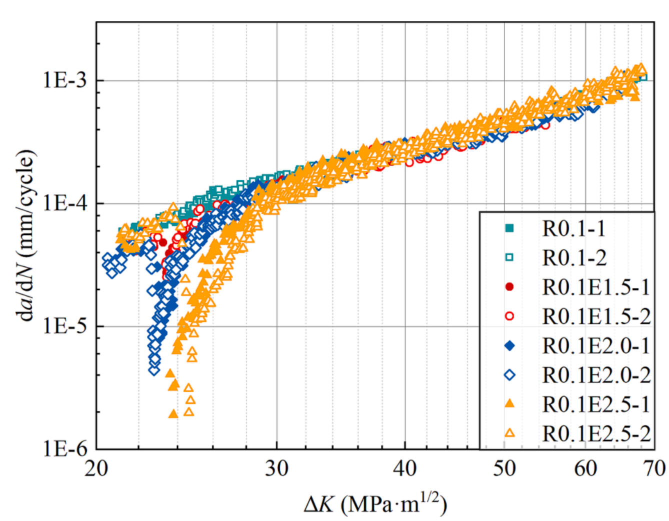

Fig. 11. FCGR curves for $R = 0.1$ conditions.

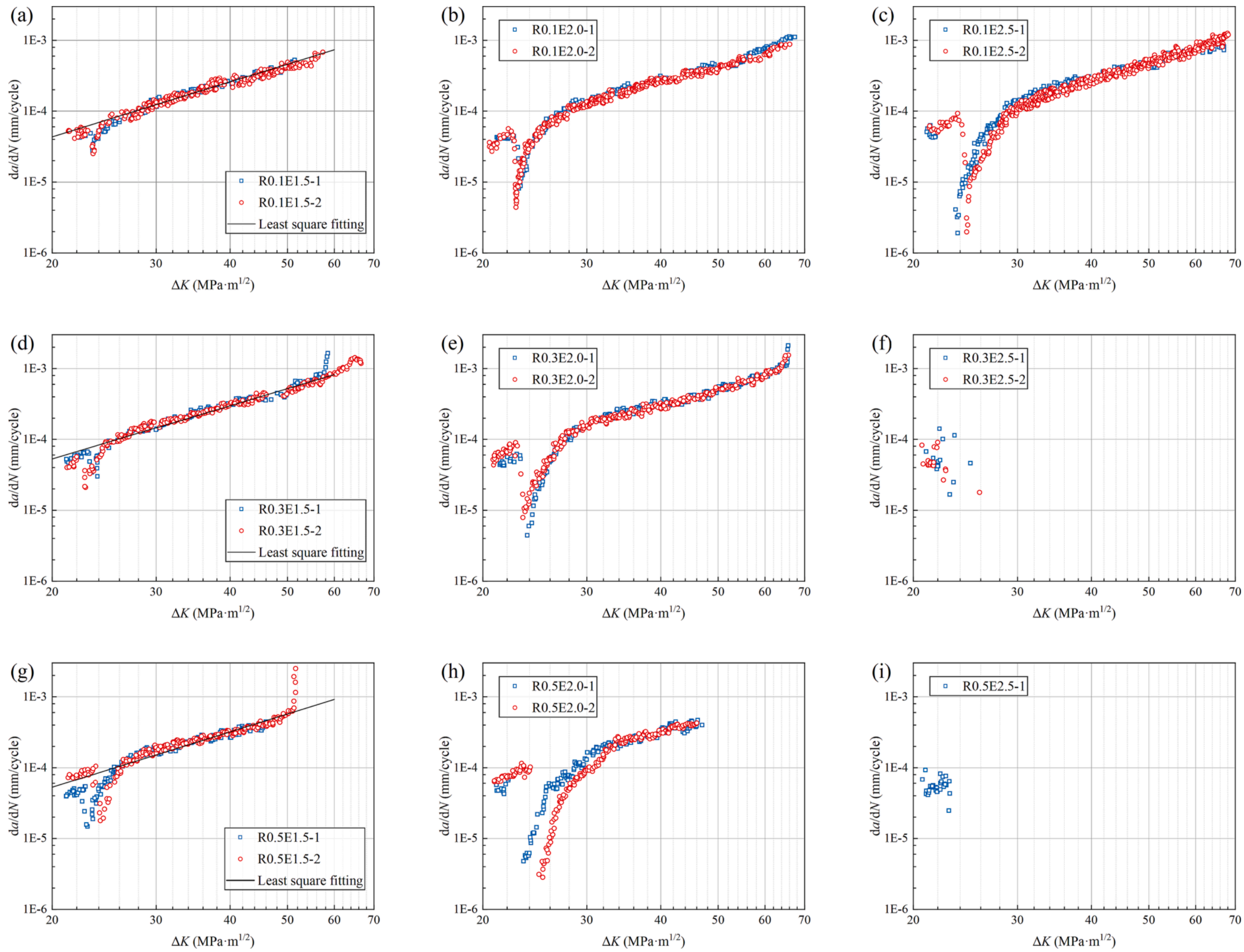

Fig. 12. D*a*/d*N* *vs.* Δ*K* curves: (a) R0.1E1.5; (b) R0.1E2.0; (c) R0.1E2.5; (d) R0.3E1.5; (e) R0.3E2.0; (f) R0.3E2.5; (g) R0.5E1.5; (h) R0.5E2.0; (i) R0.5E2.5.

identical overload ratio. It is worth mentioning that the crack arrest behavior occurred for cases R0.3E2.5 and R0.5E2.5. In other words, the fatigue cracks no longer propagate when the number of load cycles reaches more than one million under these two load conditions.

3.1.2. d*a*/d*N* vs. Δ*K* curves

The FCGR (d*a*/d*N*) at the corresponding crack length was obtained by processing the *a*-*N* curves through the incremental polynomial fitting method recommended by ASTM E647. The FCGR and SIF amplitude for $R = 0.1$ were plotted on a log-log coordinate system, as shown in Fig. 11. The results show that the FCGR decreased after a single overload, and the greater the overload ratio, the more pronounced the decreased in FCGR under the identical stress ratio. Moreover, the FCGR before a single overload and after the completion of the retardation stage was almost identical to that in the stable growth stage under constant amplitude loading.

The test results indicate that the FCG retardation behavior occurred for the CT specimens of all testing conditions after a single overload, as shown in Fig. 12. The accelerated propagation stage did not occur but decreased slowly to the minimum FCGR value after applying a single overload to the Q500qE steel. Simultaneously, the minimum FCGR decreased with the increased overload ratio applied to a single overload under the identical stress ratio. Furthermore, the FCGR could be considered zero since the fatigue crack was no longer propagated due to the single overload application for the two cases of R0.3E2.5 and R0.5E2.5. The FCGR was approximated as a curve in the log-log coordinate system when the FCGR gradually recovered from the lowest point to the stable growth stage. The FCGR eventually returned to the stable growth stage with the increase of the SIF amplitude and continued to grow until the fatigue test was completed.

Table 4
Fitting parameters in the crack stable growth region.

Fitting parameters	Stress ratios *R*		
	0.1	0.3	0.5
m	2.58	2.50	2.60
$\log C$	−7.72	−7.53	−7.66
R^2	0.964	0.966	0.926

The Paris formula is commonly used to describe the growth behavior of the fatigue crack stable growth stage in materials, as expressed in Eq. (2). The C and m values of Q500qE steel were obtained using the least squares method in the log-log coordinate system based on the tested data of the stable growth stage before and after applying a single overload, as shown in Table 4. However, the Paris formula was no longer applicable for calculating the FCGR during the entire retardation stage. Therefore, the overload retardation model should be modified based on the Paris formula.

Table 5
Retardation parameters of single overload tests.

Specimen number	a_{OL}(mm)	N (cycle)	$(da/dN)_{be,max}$ (mm/cycle)	$(da/dN)_{min}$ (mm/cycle)	η	$(da/dN)_{re}$ (mm/cycle)
R0.1E1.5–1	7.858	89,000	3.05×10^{-5}	2.74×10^{-5}	0.8984	5.61×10^{-5}
R0.1E1.5–2	7.880	83,892	3.17×10^{-5}	2.51×10^{-5}	0.7917	6.92×10^{-5}
R0.1E2.0–1	7.743	116,962	3.07×10^{-5}	8.08×10^{-6}	0.2632	1.08×10^{-4}
R0.1E2.0–2	7.868	124,318	5.60×10^{-5}	4.42×10^{-6}	0.0789	1.11×10^{-4}
R0.1E2.5–1	8.330	236,204	4.28×10^{-5}	1.90×10^{-6}	0.0444	1.43×10^{-4}
R0.1E2.5–2	7.607	197,645	9.30×10^{-5}	1.98×10^{-6}	0.0213	1.32×10^{-4}
R0.3E1.5–1	8.019	74,299	6.64×10^{-5}	2.97×10^{-5}	0.4473	1.01×10^{-4}
R0.3E1.5–2	8.157	68,996	5.35×10^{-5}	$2.10\times10_{-5}$	0.3925	1.01×10^{-4}
R0.3E2.0–1	7.929	129,055	6.14×10^{-5}	4.39×10^{-6}	0.0715	1.83×10^{-4}
R0.3E2.0–2	8.106	117,593	9.00×10^{-5}	7.91×10^{-6}	0.0879	1.90×10^{-4}
R0.3E2.5–1	7.983	>1,000,000	2.48×10^{-5}	–	–	–
R0.3E2.5–2	8.240	>1,000,000	3.80×10^{-5}	–	–	–
R0.5E1.5–1	7.809	82,781	5.38×10^{-5}	1.47×10^{-5}	0.2732	1.19×10^{-4}
R0.5E1.5–2	8.225	69,038	1.05×10^{-4}	1.79×10^{-5}	0.1705	1.23×10^{-4}
R0.5E2.0–1	7.827	533,233	6.91×10^{-5}	4.76×10^{-6}	0.0689	1.70×10^{-4}
R0.5E2.0–2	8.374	410,850	1.02×10^{-4}	2.84×10^{-6}	0.0278	2.23×10^{-4}
R0.5E2.5–1	7.821	>1,000,000	6.39×10^{-5}	–	–	–

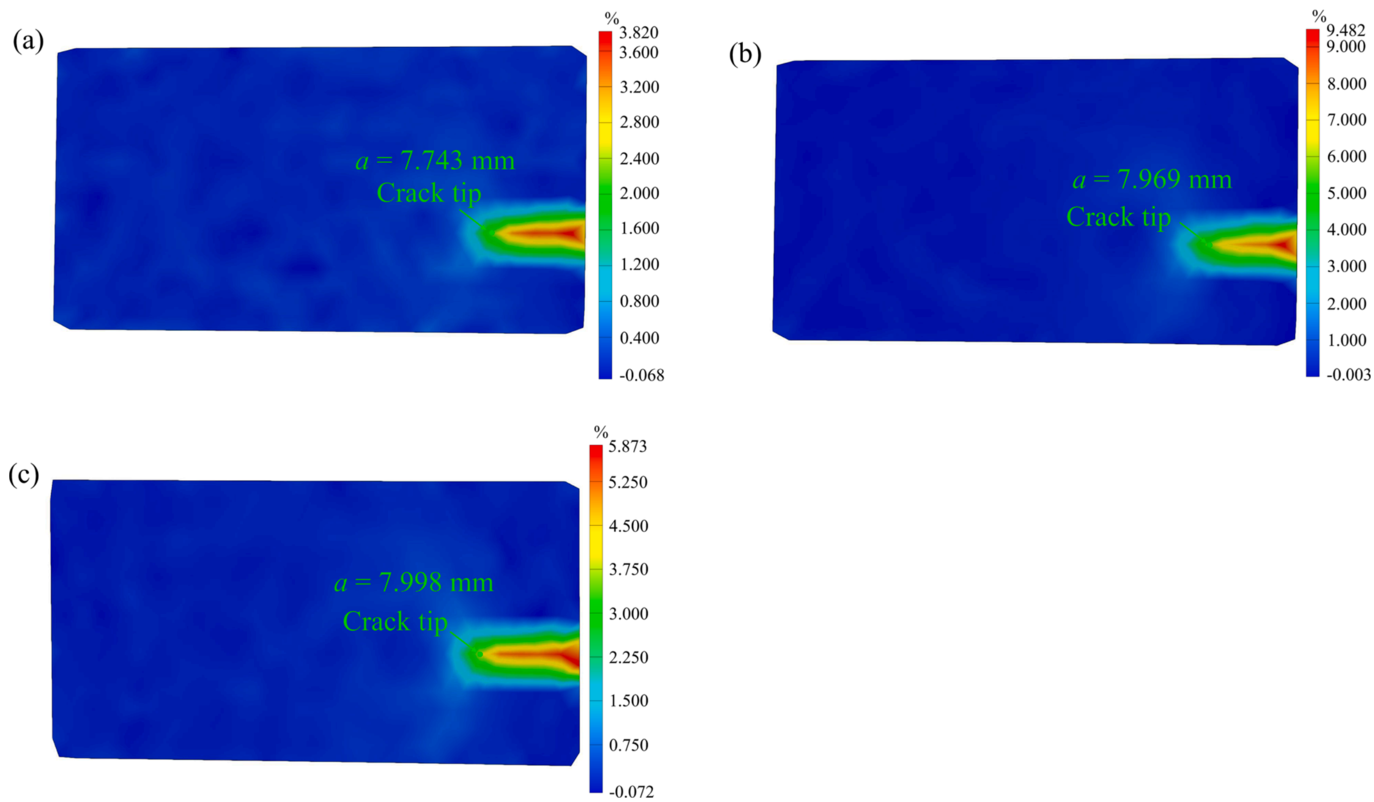

Fig. 13. Strain distribution in the y direction at the crack tip for R0.1E2.0–1: (a) $P_{max} = 4$ kN corresponding to $a = 7.743$ mm; (b) $P_{OL} = 8$ kN corresponding to $a = 7.969$ mm; (c) $P = 4$ kN after a single overload corresponding to $a = 7.998$ mm.

$$\frac{da}{dN} = C(\Delta K)^m \tag{2}$$

where C and m represent the material constants.

The important FCG parameters during the retardation stage after a single overload are summarized in Table 5. Furthermore, a dimensionless constant η was defined to characterize the retardation effect intensity and degree of retardation, as expressed in Eq. (3).

$$\eta = \frac{(da/dN)_{min}}{(da/dN)_{be,max}} \tag{3}$$

where $(da/dN)_{min}$ and $(da/dN)_{be,max}$ represent the minimum FCGR after and before single overloads, respectively. The results of Fig. 12 and Table 5 show that the smaller the retardation coefficient η is, the stronger the retardation effect is under the identical stress ratio, i.e., the smaller the minimum value of the FCGR that can be achieved after applying a single overload. In addition, the smaller the retardation coefficient η is, the greater the delay of the FCGR is under the identical overload ratio, i.e., the higher the number of load cycles in the delayed retardation stage after applying a single overload.

3.2. Deformation fields at crack tip

Fig. 13 shows the crack tip strain distributions for the specimen R0.1E2.0–1 calculated by the DIC measurement, corresponding to the maximum load P_{max} before the applied single overload, the overload P_{OL}, and the load P after applying single overload during constant

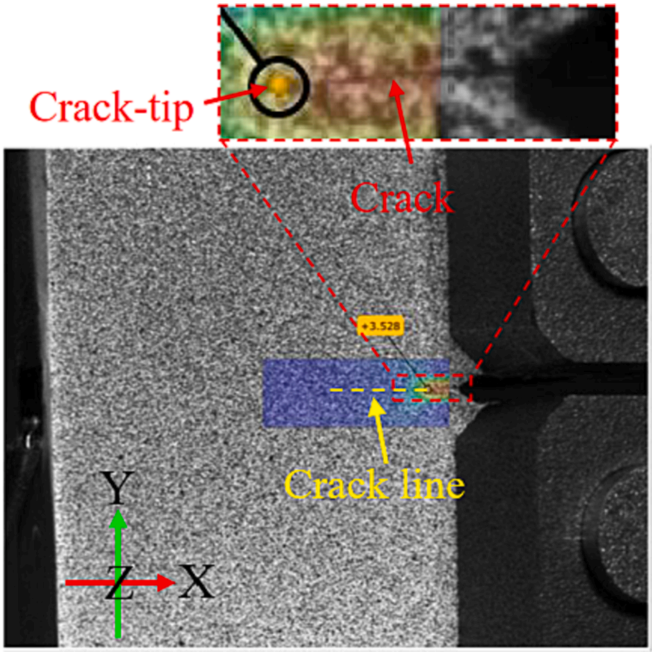

Fig. 14. Crack line in front of crack tip.

amplitude loading, respectively. The results show that the strain near the crack tip was about 2.80 % for the maximum load $P_{max} = 4$ kN before applying single overload. When the load increased to an overload value $P_{OL} = 8$ kN, the strain near the crack tip was about 7.00 %. It can be seen that the plastic deformation of the crack tip due to the single overload was more than two times that during constant amplitude loading. The crack tip strain, which did not return to the strain level before applying single overload, was about 4.50 % when the overload was unloaded to $P = 4$ kN, indicating that the residual strain (i.e., residual plastic deformation) near the crack tip was caused by the overload.

To further investigate the deformation field before the crack tip of Q500qE steel after a single overload, one specimen was selected from each work condition using a DIC measurement system to capture the strain field images around the crack tip, as shown in Fig. 14. Subsequently, a rectangular region that contained the crack tip was selected from the collected images for strain calculation. Next, a crack line was constructed directly ahead of the crack tip to extract the numerical values of longitudinal strain ε_{yy} at different positions along the crack growth path.

Fig. 15(a) shows the strain distribution measured by DIC during a single overload for $R = 0.1$ and OLR = 1.5, 2.0, and 2.5. The digital image obtained during the stable growth stage before the application of overloading was taken as the reference image (i.e., point A). Then, the strain values during a single overload cycle (A-B-C) were calculated based on point A, and strain evolution throughout the process was analyzed. The results indicate that the crack tip exhibited the maximum strain when the maximum overload was applied (i.e., point B), and the strain at this location increased with increasing overload ratio under the identical stress ratio. When the force was unloaded to the minimum value (i.e., point C) after a single overload, the strain values at the crack tip for OLR = 1.5, 2.0, and 2.5 were 0.01 %, 0.09 %, and 1.46 %, respectively. It indicated that the strain at the crack tip did not fully recover to the pre-overloading level after the single overload was completed, but instead generated a certain amount of residual strain. The variation of residual strain with time and distance during a single overload ahead of the cracked tip was further analyzed using R0.1E2.5 as an example. Then, strain data were extracted along the crack line to plot a three-dimensional strain distribution, as shown in Fig. 15(b). The results show that there was a high level of strain near point B. In addition, the further the distance from the crack line to the crack tip, the lower the residual strain values, and there was hardly any residual strain beyond a certain distance.

Previous studies [15,42] have shown a close relationship between the strain distribution ahead of the crack tip and the mechanism of residual stress (plastic deformation). Therefore, the digital image of the

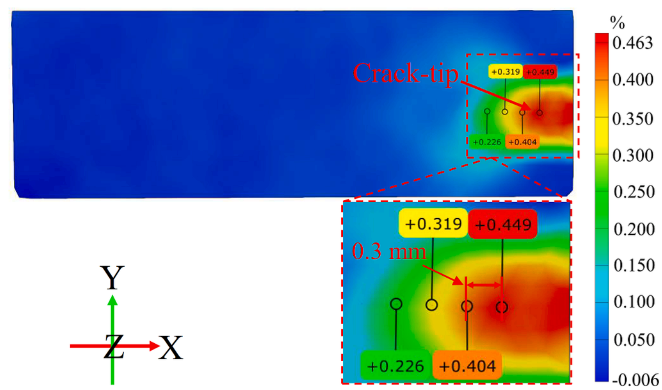

Fig. 16. Strain nephogram of overload unloading to P_{min}.

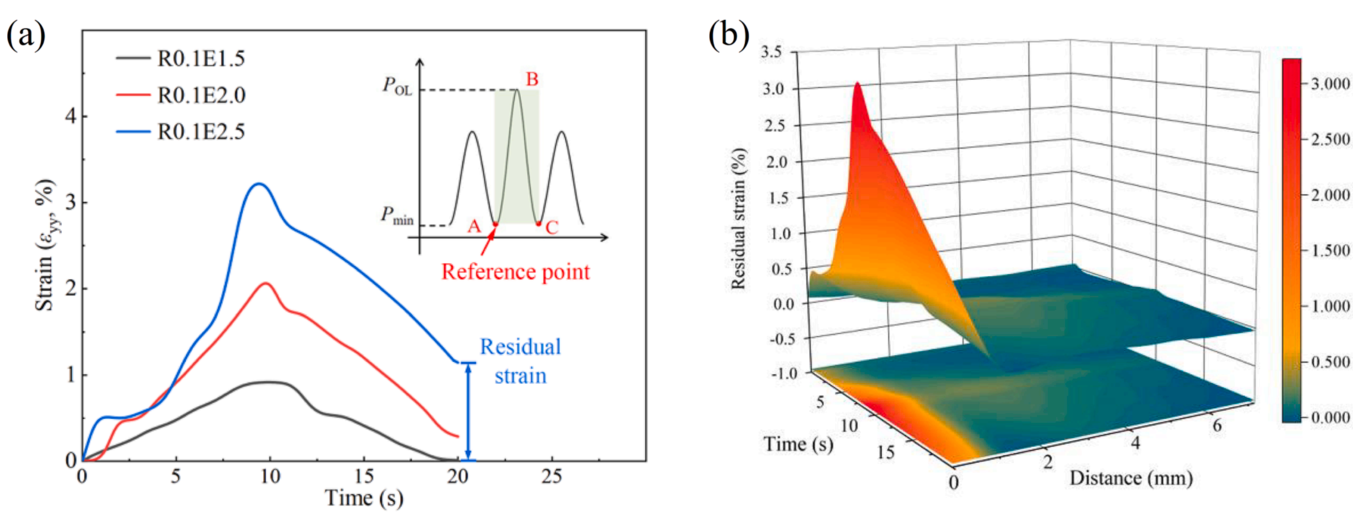

Fig. 15. Strain distribution at crack tip in the *y* direction during single overload: (a) crack tip strain evolution at R = 0.1; (b) evolution of crack tip strain with time and distance for R0.1E2.5.

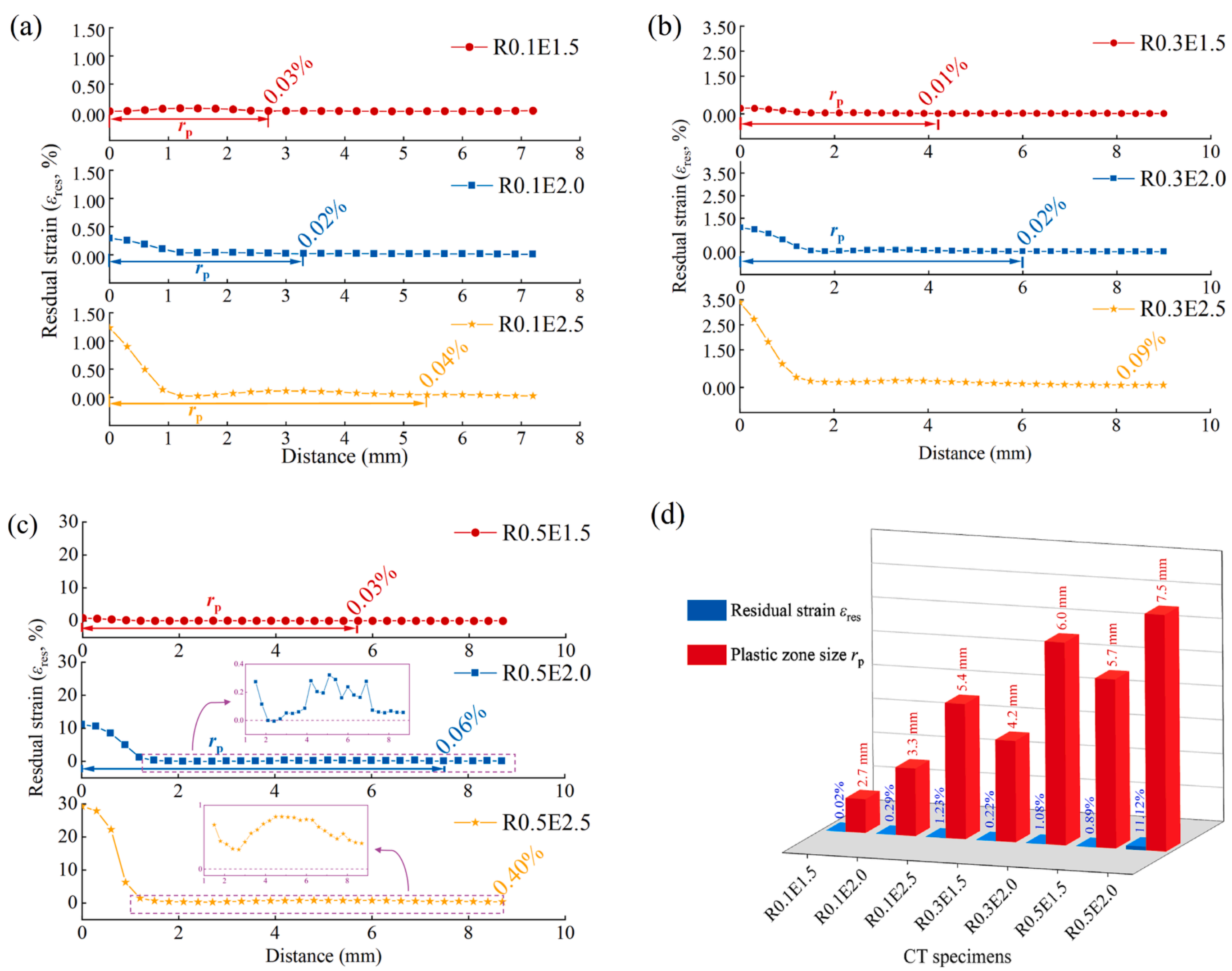

Fig. 17. Residual strain distribution along the ahead of crack tip in the y direction under different stress ratio: (a) $R = 0.1$; (b) $R = 0.3$; (c) $R = 0.5$; (d) crack tip strain parameters.

P_{min} (i.e., point C) after the completion of a single overload obtained by a DIC was processed. The strain values ε_{yy} of the Y direction were extracted by setting a calculation point with every 0.3 mm along the crack line (i.e., negative X direction) starting from the crack tip, as shown in Fig. 16.

Fig. 17(a – c) shows the strain distribution ahead of the crack tip in

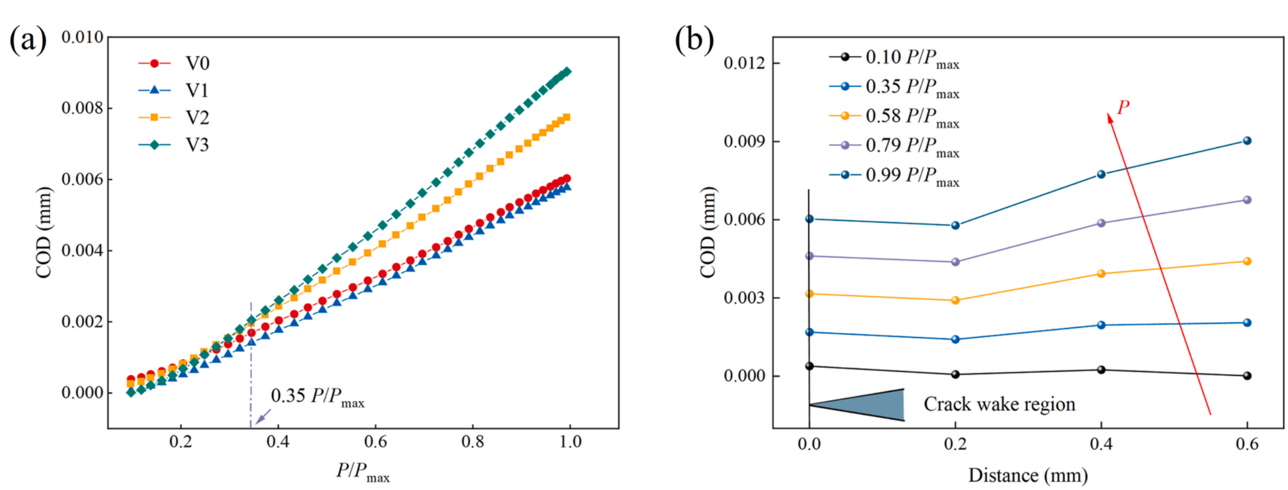

Fig. 18. Crack closure behavior of the crack wake region under constant amplitude loading: (a) crack opening distance and P/P_{max} relationship; (b) COD variation corresponds to a specific distance.

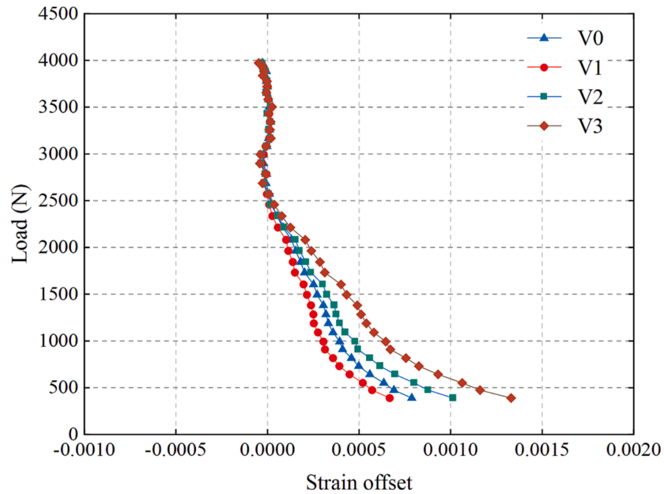

Fig. 19. Load *vs.* crack opening offset curves at different locations.

the y direction under R = 0.1, 0.3, and 0.5 after unloading the single overload. The test results indicated that the residual strain first exhibited a gradient decrease trend along the crack propagation direction. Subsequently, it showed a trend of increasing, then decreasing, and gradually stabilizing. However, the case R0.1E1.5 did not exhibit a gradient decrease. Furthermore, the residual strain increased and then exhibited fluctuating changes before decreasing for case R0.5E2.0. Previous studies [40] have shown that plastic deformation at the crack tip was caused by a single overload and resulted in the residual strain being generated in a particular region ahead of the crack tip. Therefore, the plastic zone size generated by a single overload was defined as the distance ranges from the crack tip to the point where the residual strain was closed to the 0 % line in this study [39,40]. For example, the residual strain of case R0.1E2.0 at a distance of 3.3 mm from the crack tip was monotonically decreased to 0.02 %; thus, the plastic zone size r_p was 3.3 mm. To quantitatively analyze the deformation field at the crack tip under different stress and overload ratios, the residual strain ε_{res} and plastic size r_p at the crack tip after a single overload were counted, as shown in Fig. 17(d). It is worth noting that the cases of R0.3E2.5 and R0.5E2.5 were not counted. The residual strain decreased to the 0.90 % point that the distance from the crack tip was 8.4 mm for case R0.3E2.5, exceeding the crack propagation length (a = 8.106 mm). Similarly, there was still 0.40 % residual strain present at a distance of 9 mm from the crack tip for the case R0.5E2.5. These results of the two cases indicate that a larger plastic deformation at the crack tip was generated by a tensile overload, resulting in the driving force generated by subsequent fatigue loading being insufficient to cause the crack to pass through this plastic zone, leading to the crack arrest behavior. In addition, the residual strain and plastic zone size increased with increasing overload ratios for all other stress ratios under identical stress ratios.

3.3. Crack closure response at crack tip wake region

Fig. 18(a) presents the crack opening displacement (COD) variation at specific locations in the crack tip and crack wake region of R0.1E2.5

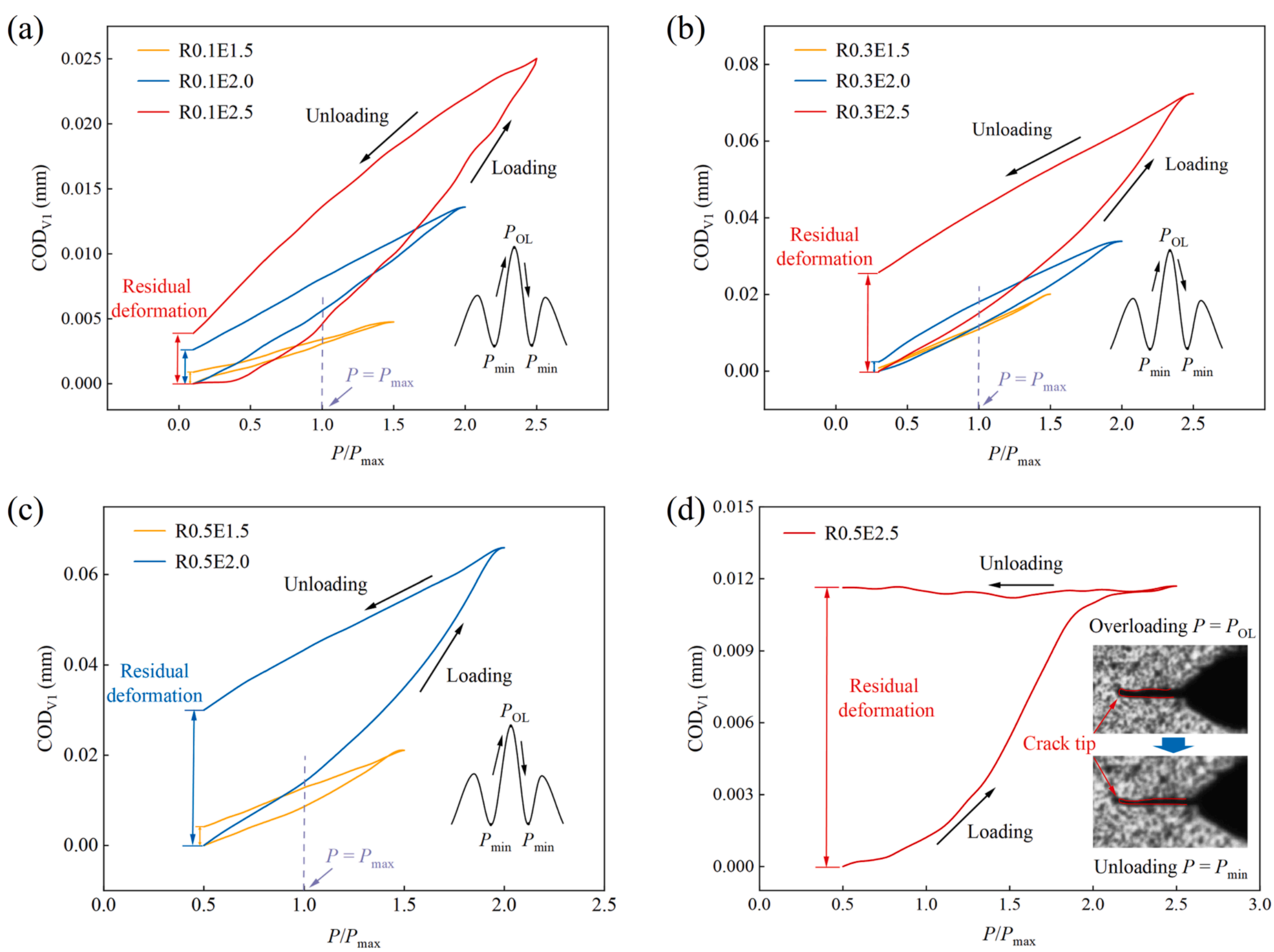

Fig. 20. Crack closure behavior during a single overload: (a) R = 0.1; (b) R = 0.3; (c) R = 0.5; (d) R0.5E2.5.

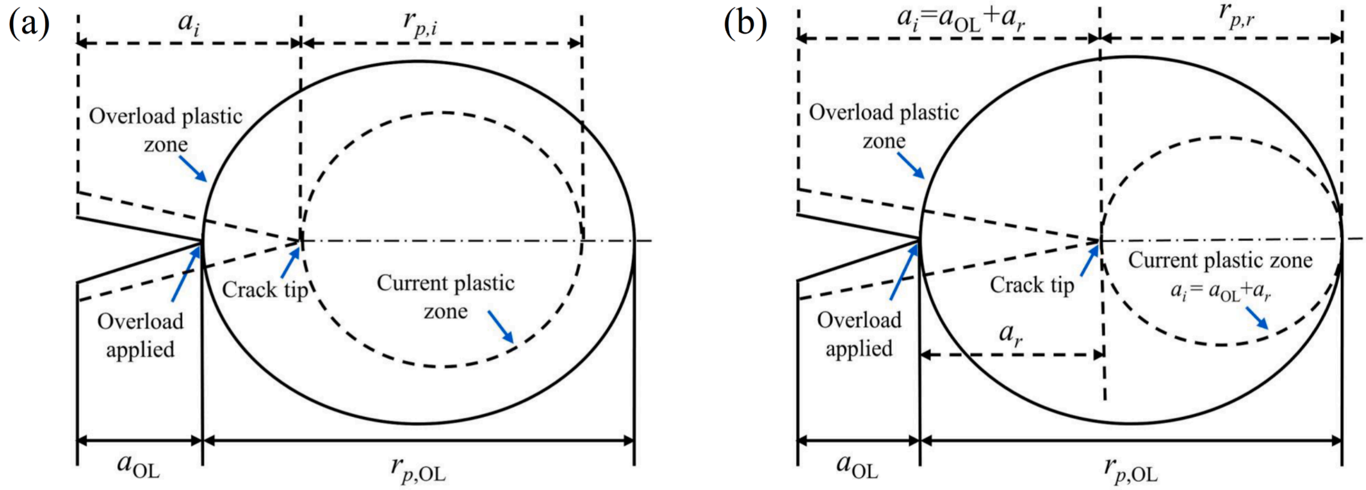

Fig. 21. Schematic of retardation parameters: (a) the crack length at a_i, (b) the crack length at $a_i = a_{OL} + a_r$.

during the constant amplitude loading stage before applying a single overload. The results show that the COD increased slowly with load ratio P/P_{max} before $0.35P/P_{max}$, while it showed a linear growth trend after exceeding 0.35 P/P_{max}, indicating that there is a closure effect to resist crack opening during the crack opening process. Furthermore, it was found that the COD at the crack tip (V0) was greater than that V1 under the identical P/P_{max}, indicating that the COD variation at the crack tip was more sensitive to force changes. Fig. 18(b) shows the COD variations at a specific distance in the crack wake region. It can be seen that the COD variation exhibited a more significant variation with increasing distance after exceeding 0.35 P/P_{max}, indicating that the crack was fully open at this time, further demonstrating the existence of crack closure effect in the constant amplitude loading stage of Q500qE steel.

To further clarify the crack opening force values and the crack closure response at different locations in the crack wake region during the constant amplitude loading stage, the strain offset method [43,44] was employed to process the COD and P/P_{max} data of Fig. 18(a). The strain offset was calculated by Eq. (4).

$$\text{strain offset} = [\text{COD}]_{\text{THE}} - [\text{COD}]_{\text{EXP}} \tag{4}$$

where $[\text{COD}]_{\text{THE}}$ and $[\text{COD}]_{\text{EXP}}$ are the theoretical and experimental strains, respectively. For this purpose, a force-strain data segment with a span of about 25 % of the cyclic load range starting from the maximum force was selected, and a least squares method was used for fitting. Then, the $[\text{COD}]_{\text{THE}}$ corresponding to each load value was calculated based on the fitting formula.

The relationship between the load and crack opening offset at different locations in the crack wake region was obtained, as shown in Fig. 19. The *x*-axis represented the strain offset, and the crack was fully opened when the strain offset beyond zero, indicating that the crack closure effect was no longer practical. Therefore, the load corresponding to a slightly higher than zero strain offset value was defined as the crack opening load. The crack opening loads were 2686.3 N, 2336.4 N, 2457.5 N, and 2570.7 N, respectively, corresponding to V0, V1, V2, and V3 when $a = 7.66$ mm. The results show a close relationship between the crack opening load and the arrangement of virtual extensometers in the crack wake region, and the strain offset increased as the distance from the crack tip increased. However, the calculated crack opening load was 2686.3 N based on the virtual extensometer arranged at the crack tip higher than the calculated crack opening load of others. Previous studies [40,44] have shown that virtual extensometers closer to the crack tip were more effective in reflecting the local crack closure effect in the crack wake region. However, it was unsatisfactory to place them at the crack tip, causing significant calculation errors. Therefore, a virtual extensometer located 0.2 mm behind the crack tip was selected to calculate the COD (i.e., COD_{V1}) corresponding to the load value based on tested errors and computational accuracy in this study. This is because it could better reflect the crack closure response in the crack wake region.

Fig. 20 shows the relationship between COD_{V1} and P/P_{max} in the crack wake region during a single overload under the stress ratio $R =$ 0.1, 0.3, and 0.5. The results show that the COD_{V1} variation exhibited a relatively gentle trend with the P/P_{max} when the OLR was small. This is attributed to the new plastic zone generated during the overload loading stage ($P > P_{max}$) changed relatively minor compared to the constant amplitude loading stage, resulting in lower resistance when the material at the crack tip undergoes elastic recovery. Therefore, the shielding effect at the crack tip hardly increased, leading to weaker crack closure exhibited under low overload levels. The COD_{V1} increased slowly with the P/P_{max} when $P < P_{max}$ for the OLR = 2.5 and showed a linear growth trend when $P > P_{max}$. However, the COD_{V1} increased linearly with the P/P_{max} when $P < P_{max}$ for the OLR = 1.5 and 2.0, indicating that the crack tip was weakly affected by crack closure at this condition. Therefore, it can be concluded that the larger the overload ratio, the stronger the retardation effect under the identical stress ratio.

Additionally, the residual deformation in the crack wake region increased with the overload ratios under the identical stress ratio after a single overload unloading. This is because a new sizeable plastic deformation region was generated near the crack tip when the load value reached P_{OL}, leading to a lower degree of linear elastic recovery of the surrounding material during crack closure. Thus, a large residual deformation in the wake region was generated after a single overload. It took sufficient load cycles to eliminate the shielding effect generated at the crack tip returning to the constant amplitude loading stage. The shielding effect refers to the plastic deformation or deformation model change occurring locally at the crack tip to reduce stress concentration and FCGR [40]. The large residual deformation suppressed the closure of the crack surface in the region, decreasing the sharpness of the crack tip and stress concentration. Therefore, this further demonstrated that the larger the overload force, the stronger the shielding effect at the crack tip and the greater the ability to retard crack growth. In particular, the crack wake region was no longer closed due to the sizeable residual plastic deformation for the R0.3E2.5 case. Furthermore, the opening displacement behind the crack was insignificant when the load increased to P_{OL} for the R0.5E2.5 case, but the opening displacement hardly changed during the unloading stage. The maximum residual deformation was 0.012 mm, also lower than 0.030 mm under the R0.3E2.5 condition. This may be due to the blunting effect at the crack tip, as shown in Fig. 20 (d). It depicted the crack tip shape corresponding to P_{OL} during a single overload and P_{min} after overload unloading. The singularity of the stress field at the crack tip disappeared due to the blunting effect, resulting in a reduction of the local stress concentration effect at the crack tip during the constant amplitude loading stage after a single overload. This behavior significantly reduced the driving force of crack propagation and even led to crack arrest phenomenon generation during the fatigue crack propagation.

4. FCGR retardation model

4.1. Modified Wheeler model

Wheeler [32] introduced a retardation parameter ϕ_R to describe the retardation behavior after overloading based on the Paris model, as expressed in Eq. (5).

$$\frac{da}{dN} = \phi_R[C(\Delta K)^m] \tag{5}$$

where C and m represent material constants fitted by the Paris equation. The retardation coefficient ϕ_R is a function of the plastic zone size, as expressed in Eq. (6).

$$\phi_R = \begin{cases} \left[\dfrac{r_{p,i}}{a_{OL} + r_{p,OL} - a_i}\right]^{m_{org}} & \text{when } a_i + r_{p,i} < a_{OL} + r_{p,OL} \\ 1 \text{ when } a_i + r_{p,i} \geqslant a_{OL} + r_{p,OL} \end{cases} \tag{6}$$

where a_i is the current crack length, a_{OL} is the crack length applied the overload, $r_{p,i}$ is the plastic zone size at the current crack length, $r_{p,OL}$ is the plastic size applied the overload, and m_{org} is a dimensionless shape parameter acquired by fitting tested data. The schematic diagram of retardation parameters of the plastic zone at the crack tip is shown in Fig. 21(a).

Sheu et al. [45] considered that the retardation effect occurred within the effective plastic zone generated by a single overload, thus the Eq. (7) was proposed for calculating the plastic zone size.

$$r_{p,i} = \alpha\left(\frac{K_i}{\sigma_{ys}}\right)^2 \tag{7}$$

where α is the plastic factor of the retardation region, K_i is the SIF at the current crack length, and σ_{ys} is the yield strength of the material. The α could be calculated by Eq. (8).

$$a_r = \alpha\left[\left(\frac{K_{OL}}{\sigma_{ys}}\right)^2 - \left(\frac{K_r}{\sigma_{ys}}\right)^2\right] \tag{8}$$

where K_{OL} is the maximum SIF applied overload, K_r is the maximum SIF corresponding to the crack length at the end of the retardation stage, a_r is the crack length from the application of the overload to the end of the retardation stage, which was obtained by the fatigue test. The schematic diagram of retardation parameters at the end of the retardation stage, as shown in Fig. 21(b).

Generally, the Wheeler model was only suitable for predicting the FCGR during the retardation stage, while it had limitations in predicting the FCGR during the delayed retardation stage. Therefore, Yuen and Taheri [8] proposed a modified model based on the Wheeler model and the theory of crack tip plasticity to predict the FCGR during the whole retardation stage simultaneously, as shown in Eq. (9).

$$\frac{da}{dN} = \phi_D \cdot \phi_R[C(\Delta K)^m] \tag{9}$$

where the delayed retardation parameter ϕ_D could be calculated by Eq. (10).

$$\phi_D = \begin{cases} \left[\dfrac{a_{OL} + r_{d,OL} - a_i}{r_{d,i}}\right]^{m\ mod} & \text{when } a_i + r_{d,i} < a_{OL} + r_{d,OL} \\ 1 \text{ when } a_i + r_{d,i} \geqslant a_{OL} + r_{d,OL} \end{cases} \tag{10}$$

where $r_{d,OL}$ is the plastic zone size of the delayed retardation stage, $r_{d,i}$ is the plastic zone size at the current crack length in the delayed retardation stage, m_{mod} is the shape parameter of the modified model. The $r_{d,i}$ was calculated by Eq. (11).

$$r_{d,i} = \beta\left(\frac{K_i}{\sigma_{ys}}\right)^2 \tag{11}$$

where, β is the plastic zone of the delayed retardation stage, which could be calculated by Eq. (12).

$$a_d = \beta\left[\left(\frac{K_{OL}}{\sigma_{ys}}\right)^2 - \left(\frac{K_d}{\sigma_{ys}}\right)^2\right] \tag{12}$$

where, a_d is the crack length of the delayed retardation stage, which is the interval from the crack length when overload is applied to the crack length when FCGR reaches the lowest.

It is necessary to fit a high-precision shape parameter m_{org} through tested data and to calculate the α accurately when using the FCGR prediction model after a single overload. However, there are currently no unified formulas suitable for calculating the plastic zone parameters for all materials due to the significant differences in mechanical behavior among different materials. Therefore, the actual plastic zone size obtained by the DIC measurement was used to calculate the plastic zone parameters based on the modified Wheeler model proposed by Yuen and Taheri [8] in this study. Then, a high-precision prediction model that can calculate the FCGR during both the delayed retardation stage and the retardation stage was proposed.

4.2. Validation of modified Wheeler model

It is worth noting that some loading conditions (such as R0.1E2.0) were able to acquire the FCFR data in the delayed retardation stage, while some loading conditions (such as R0.1E2.5–2, R0.3E2.0–1 and R0.5E2.5) were not acquired. Therefore, this study will focus on the two representative situations of R0.1E2.0 and R0.1E2.5 for calculation based on the modified Wheeler model. Firstly, the plastic zone factors α for R0.1E2.0 and R0.1E2.5 were calculated by Eq. (7), respectively, using the plastic zone size obtained from the tests when the overload was applied. Then, the Eq. (13) was obtained by taking the logarithms on both sides of Eq. (5) and Eq. (6).

$$\lg\phi_{R,modified} = \lg\left(\frac{da}{dN}\right)_{EXP,R} - \lg\left(\frac{da}{dN}\right)_{CAL,R} \tag{13}$$

where, $\phi_{R,modified}$ is the modified retardation parameter; $\lg\left(\frac{da}{dN}\right)_{EXP,R}$ and $\lg\left(\frac{da}{dN}\right)_{CAL,R}$ are tested and calculated FCGR values in the retardation stage, respectively.

The shape index α was obtained by fitting the data acquired by Eq. (6) and Eq. (13). However, the FCGR variation in the retardation stage exhibited a curved pattern. The variation trend was relatively smooth, as shown in Fig. 12. A similar experimental phenomenon was observed by Lu et al. [36] in the investigation of the FCG behavior after a single overload for steel QSTE340TM. They introduced a logistic sigmoid function to characterize the variation smooth process of FCGR curves when establishing a retardation mode. Therefore, to modify the retardation coefficient of this study, the logistic sigmoid function, as expressed in Eq. (14), was introduced to calculate the theoretical FCGR during the retardation stage.

$$\xi = \frac{1}{1 + e^{-\lambda\omega}} \tag{14}$$

where λ is the coefficient to describe the excessive smoothness of the FCGR curve during the retardation stage, usually defined as 50 – 100, ω is a dimension constant that characterizes the crack length variation

Table 6
Calculation parameters during the retardation stage.

Specimen number	a_{OL} (mm)	K_{OL} (N/mm$^{3/2}$)	$r_{p,OL}$ (mm)
R0.1E2.0–1	8.330	2110.78	5.4
R0.1E2.5–1	7.743	1598.60	3.6

after applying a single overload, as expressed in Eq. (15).

$$\omega = \frac{a_i - a_{OL}}{a_{OL}} \tag{15}$$

where a_i and a_{OL} are the current crack length after applying the overload and the crack length when applied to the overload, respectively. In conclusion, the FCGR during the retardation stage was calculated by Eq. (16).

$$\frac{da}{dN} = \xi \cdot \phi_{R,\mathrm{modified}} \cdot C(\Delta K)^m \tag{16}$$

The key parameters of calculating the retardation stage for R0.1E2.0 and R0.1E2.5 cases are summarized in Table 6.

The plastic zone factors α and shape index m_{org} for R0.1E2.0 and R0.1E2.5 were 0.64, 0.88, and 0.55, 0.63, respectively. Furthermore, the material constants were acquired by fitting the tested data (as shown in Fig. 12) of the constant amplitude stable growth stage when the stress ratio $R = 0.1$, and the values of C and m were 1.91×10^{-8} and 2.58, respectively. Fig. 22 shows FCGR prediction curves estimated by the modified Wheeler model on Q500qE steel. The results indicate that the FCGR during the retardation stage was predicted by the modified Wheeler model effectively. However, there was a deviation in calculating the minimum FCGR after a single overload. Therefore, the FCGR of the R0.1E2.0 specimen was calculated by a modified Wheeler model to further investigate the minimum FCGR and the FCGR during the delayed retardation stage.

Firstly, the delayed retardation parameters ϕ_D and the plastic zone factor β during the delayed retardation stage were calculated by Eq. (10) and Eq. (12), respectively. The key parameters of calculating for R0.1E2.0 are summarized in Table 7.

The value of β was calculated to be 0.05. Subsequently, the fitting equation for calculating the shape index m_{mod} during the delayed retardation stage was obtained by taking the logarithm of both side of Eq. (9) and Eq. (10), as expressed in Eq. (17).

$$\lg\left(\frac{da}{dN}\right)_{EXP,D} - \lg\left(\frac{da}{dN}\right)_{CAL,D} = \lg\phi_R + m_{mod} \cdot \lg\left(\frac{a_{OL} + r_{d,OL} - a_i}{r_{d,i}}\right) \tag{17}$$

where $\lg\left(\frac{da}{dN}\right)_{EXP,D}$ and $\lg\left(\frac{da}{dN}\right)_{CAL,D}$ are the tested and calculated FCGR during the delayed retardation stage. Here, $\lg\phi_R$ was actually replaced by Eq. (13). Therefore, the FCGR during the delayed retardation stage could be calculated by Eq. (18).

$$\frac{da}{dN} = \xi \cdot \phi_D \cdot \phi_{R,\mathrm{modified}} \cdot [C(\Delta K)^m] \tag{18}$$

In conclusion, the equation that calculated the FCGR of the whole cyclic loading stage, including stable growth stage, delayed retardation stage, and retardation stage, was obtained, as expressed in Eq. (19).

$$\frac{da}{dN} = \begin{cases} C(\Delta K)^m a_i \leqslant a_{OL}, a_{OL} + r_{p,OL} - r_{p,i} < a_i \\ \xi \cdot \phi_D \cdot \phi_{R,\ modified} \cdot [C(\Delta K)^m] a_{OL} < a_i \leqslant a_{OL} + r_{d,OL} - r_{d,i} \\ \xi \cdot \phi_{R,\ modified} \cdot [C(\Delta K)^m] a_{OL} + r_{d,OL} - r_{d,i} < a_i \leqslant a_{OL} + r_{p,OL} - r_{p,i} \end{cases} \tag{19}$$

The FCGR prediction curve and tested values for R0.1E2.0 are shown in Fig. 23. The results show that the minimum FCGR calculated was 7.85×10^{-6} mm/cycle after introducing the delayed retardation coefficient ϕ_D into the modified Wheeler model, while the minimum FCGR from the tested data was 8.08×10^{-6} mm/cycle. The error between the calculated value and the tested value was 2.85 %. Furthermore, the modified Wheeler model has a nonnegligible errors in predicting the

Table 7
Calculation parameters during the delayed retardation stage.

Specimen number	$a_{\min(da/dN)}$ (mm)	a_d (mm)	K_d (N/mm$^{3/2}$)	$r_{d,OL}$ (mm)
R0.1E2.0–1	8.239	0.632	837.22	0.31

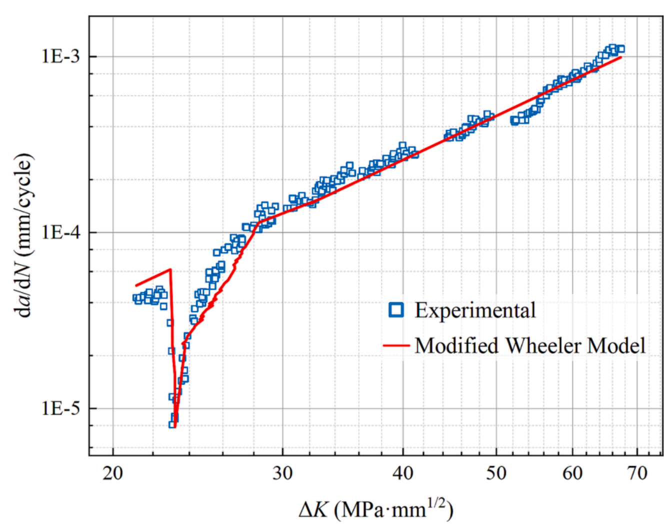

Fig. 23. FCGR prediction curve by the modified Wheeler model.

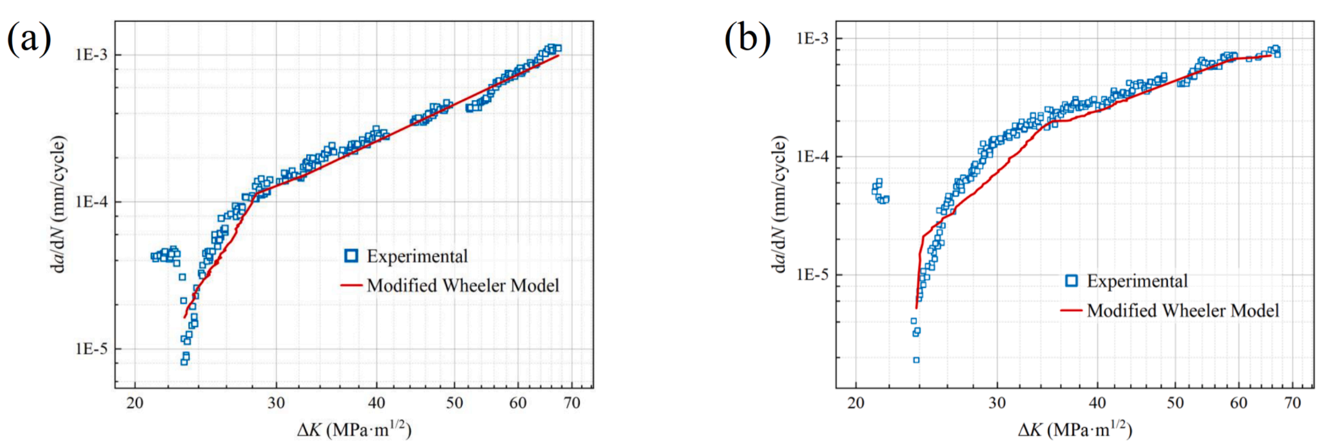

Fig. 22. FCGR prediction curves of the retardation stage calculated by the Wheeler model: (a) R0.1E2.0, (b) R0.1E2.5.

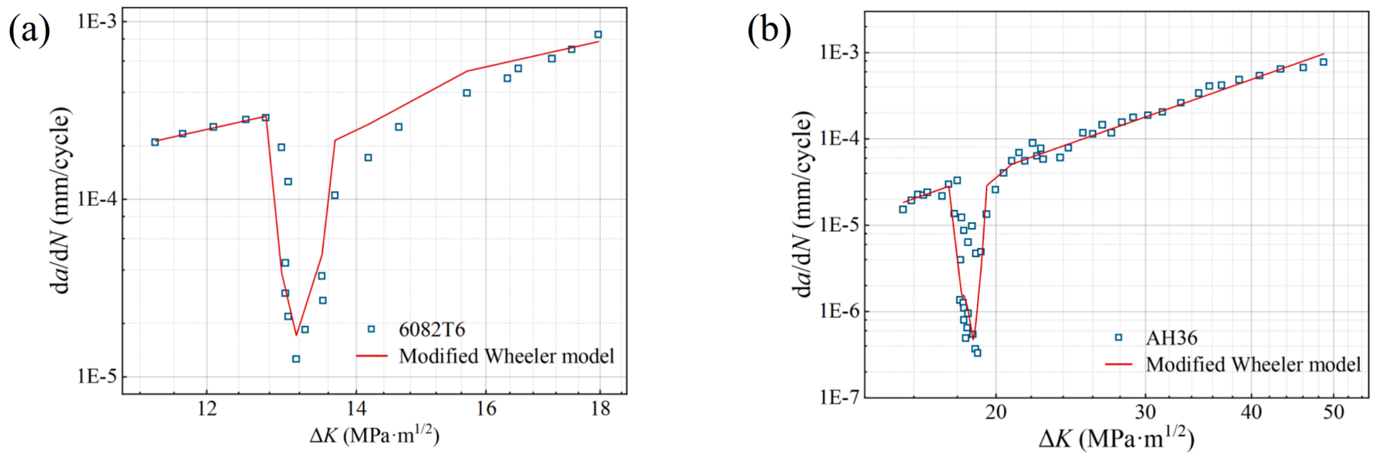

Fig. 24. Application effect of Modified Wheeler model: (a) 6082T6 aluminum, (b) AH36 high-strength steel.

later stages of the retardation region, but it can reliably estimate the minimum FCGR. In addition, the proposed retardation model was based on the theory of plastic zone at the crack tip, without considering the parameters of crack closure theory. The primary reason for this is that the crack closure behavior in the retardation stage was influenced by residual stresses, resulting in an increase in the crack opening stress σ_{op} [15,36,40]. Unfortunately, it's not able to quantitatively obtain the crack closure parameters in our laboratory test condition. Therefore, it is anticipated that further optimization of this FCG retardation model can be achieved in the future research.

To examine the applicability of the modified Wheeler model on different materials, the test results after a single overload conducted on 6082T6 aluminum and AH36 high-strength steel were collected, thereby verifying its validity. Nowell et al. [46] carried out FCG tests on 6082T6 aluminum after a single overload under loading condition of $R = 0.125$, OLR = 2.0, and $P_{max} = 2$ kN. Utilizing the calculation method described in the previous section, the values of α and β were 0.97 and 1.39, respectively. The estimated performance of the modified Wheeler model for this material is illustrated in Fig. 24(a). Similarly, Tu et al. [34] investigated the FCG behavior of AH36 high-strength steel after a single overload under loading conditions of $R = 0.1$, OLR = 2.5, and $P_{max} = 6$ kN. The key parameters α and β were 0.17 and 0.11, respectively. The estimated performance of the modified Wheeler model for this material is shown in Fig. 24(b). The results indicated that the entire retardation stage of the FCGR was adequately characterized by the modified Wheeler model.

5. Conclusions

The fatigue crack growth retardation behavior of high-strength Q500qE steel after a single overload were investigated under different stress ratios and overload ratios. The influence mechanism of a single overload on FCG behavior was revealed. A modified model was established to predict the FCGR of the whole FCG stages. Moreover, the model is worth further modification in the future to predict the retardation FCGR in other materials. The following conclusions can be obtained:

1. The FCG retardation behavior of Q500qE steel was observed after a single overload. Under an identical stress ratio, the fatigue life was increased as the overload ratio increased. That is, the retardation effect was enhanced by increasing overload ratios.
2. Under an identical stress ratio, the residual strain and plastic zone size at the crack tip were increased as overload ratio increased. In particular, for cases $R = 0.3$ and 0.5, a large residual strain was produced under OLR = 2.5, resulting in insufficient driving force for the crack growth after tensile overload unloading, and the fatigue cracks were completely arrested.
3. Crack closure was observed during the constant amplitude fatigue loading and overloading stages. Furthermore, under the identical stress ratio, the residual deformation in the crack wake region was increased with the rise in overload ratios. The large residual deformation suppressed the closure of the crack surface in the wake region, leading to the reduction of FCGR.
4. A modified Wheeler model was proposed for predicting the FCGR after a single overload based on the measured plastic zone size. Despite the predicted values in the later stages of the retardation region were slightly smaller than tested values, it can reliably estimate the minimum FCGR. In addition, the model also gave reliable estimates of 6082T6 aluminum and AH 36 high-strength steel.

CRediT authorship contribution statement

Youlin Li: Software, Investigation, Formal analysis. **Lu Ke:** Project administration, Methodology, Funding acquisition, Conceptualization. **Chuanxi Li:** Writing – review & editing, Project administration. **Peng Feng:** Writing – review & editing. **Zheng Feng:** Writing – review & editing. **Mingdong Qiu:** Software.

Declaration of competing interest

The authors declare that they have no known competing financial interests or personal relationships that could have appeared to influence the work reported in this paper.

Data availability

The raw/processed data required to reproduce these findings cannot be shared at this time due to technical or time limitations.

Acknowledgments

The authors gratefully acknowledge the financial support from the National Natural Science Foundation of China [Grant Nos. 52208307, 52308157], the National Key Research and Development Program of China (Grant No. 2021YFB2600900), the Natural Science Foundation of Guangxi (2023GXNSFBA026256).

References

[1] Ke L, Zhu F, Chen Z, Feng Z, Zhou J, Li Y. Fatigue failure mechanisms and probabilistic S-N curves for CFRP–STEEL adhesively bonded joints. Int J Fatigue 2023;168:107470. https://doi.org/10.1016/j.ijfatigue.2022.107470.

[2] Wang B, Nagy W, De Backer H, Chen A. Fatigue process of rib-to-deck welded joints of orthotropic steel decks. Theor Appl Fract Mec 2019;101:113–26. https://doi.org/10.1016/j.tafmec.2019.02.015.
[3] Xin H, Correia J-A-F-O, Veljkovic M. Three-dimensional fatigue crack propagation simulation using extended finite element methods for steel grades S355 and S690 considering mean stress effects. Eng Struct 2021;227:111414. https://doi.org/10.1016/j.engstruct.2020.111414.
[4] Ke L, Li Y, Chen Z, Feng Z, Yan B, Zhu F, et al. Effect of microstructure on fatigue crack growth behavior of surface- and middle-layer materials of thick high-strength bridge steel plates. Fatigue Fract Eng M 2023;46:485–500. https://doi.org/10.1111/ffe.13879.
[5] Ke L, Li C, He J, Lu Y, Jiao Y, Liu Y. Fatigue evaluation and CFRP strengthening of diaphragm cutouts in orthotropic steel decks. Steel Compos Struct 2021;39(4):453–69. https://doi.org/10.12989/scs.2021.39.4.453.
[6] Wang C, Wang Y. Influence of distortion ratio on distortion-induced fatigue behavior of steel girder bridges. Thin Wall Struct 2023;188:110790. https://doi.org/10.1016/j.tws.2023.110790.
[7] Ke L, Wang Y, Li C, Chen Z, Feng Z, Li Y. Fatigue evaluation and structural optimization of rib-to-diaphragm connection in orthotropic steel decks. J Constr Steel Res 2023;208:107998. https://doi.org/10.1016/j.jcsr.2023.107998.
[8] Yuen B-K-C, Taheri F. Proposed modifications to the wheeler retardation model for multiple overloading fatigue life prediction. Int J Fatigue 2006;28:1803–19. https://doi.org/10.1016/j.ijfatigue.2005.12.007.
[9] Lu W, Zhang C. Contribution of overload-induced residual stress to fatigue retardation pertinent to notch geometry. Theor Appl Fract Mec 2023;127:104001. https://doi.org/10.1016/j.tafmec.2023.104001.
[10] Mohammed S-M-A-K, Bouiadjra B-B, Benyahia F, Albedah A. Analysis of the single overload effect on fatigue crack growth in AA 2024–T3 plates repaired with composite patch. Eng Fract Mech 2018;202:147–61. https://doi.org/10.1016/j.engfracmech.2018.09.008.
[11] Correia J, Carvalho H, Lesiuk G, Mourão A, Grilo L-F, de Jesus AABB. Fatigue crack growth modelling of fão bridge puddle iron under variable amplitude loading. Int J Fatigue 2020;136:105588. https://doi.org/10.1016/j.ijfatigue.2020.105588.
[12] Wang H, Zhang J, Li Y, Wang Z, Wu J. Experimental investigation of overload effects on fatigue crack growth behaviour of 7050–T7451 aluminium alloy. Fatigue Fract Eng M 2020;43:2928–42. https://doi.org/10.1111/ffe.13329.
[13] Ren D, Xue Z, Jiang Y, Hu X, Zhang Y. Influence of single overload on fatigue crack propagation behavior of the selective laser melting inconel 625 superalloy. Eng Fract Mech 2020;239:107305. https://doi.org/10.1016/j.engfracmech.2020.107305.
[14] Albedah A, Bouiadjra B-B, Mohammed S-M-A-K, Benyahia F. Fractographic analysis of the overload effect on fatigue crack growth in 2024–T3 and 7075–T6 al alloys. Int J Miner Metall Mater 2020;27:83–90. https://doi.org/10.1007/s12613-019-1896-4.
[15] Zhang C, Lu W. Unveiling contribution of overload-induced residual stress to fatigue retardation pertinent to crack closure and stress intensity. Mater Sci Eng A 2022;831:142268. https://doi.org/10.1016/j.msea.2021.142268.
[16] Wang C, Chen R, Guo S, Zhu M, Xuan F. Verification of stress transfer mechanism in fatigue crack growth under overload. Theor Appl Fract Mec 2023:104104. Doi: 10.1016/j.tafmec.2023.104104.
[17] Hemmesi K, Ellmer F, Farajian M, Varfolomeev I, Luke M. On the evaluation of overload effects on the fatigue strength of metallic materials. Procedia Struct Integrity 2022;38:401–10. https://doi.org/10.1016/j.prostr.2022.03.041.
[18] Neto D-M, Borges M-F, Antunes F-V, Jesus J. Mechanisms of fatigue crack growth in ti-6Al-4V alloy subjected to single overloads. Theor Appl Fract Mec 2021;114:103024. https://doi.org/10.1016/j.tafmec.2021.103024.
[19] Salvati E, Zhang H, Fong K-S, Song X, Korsunsky A-M. Separating plasticity-induced closure and residual stress contributions to fatigue crack retardation following an overload. J Mech Phys Solids 2017;98:222–35. https://doi.org/10.1016/j.jmps.2016.10.001.
[20] Gonzáles G-L-G, González J-A-O, Freire J-L-F. Characterization of discontinuous crack closure behavior after the application of a single overload cycle. Theor Appl Fract Mec 2021;114:103028. Doi: 10.1016/j.tafmec.2021.103028.
[21] Liang H, Zhan R, Wang D, Deng C, Xu X, Guo B. Effect of crack-tip deformation on fatigue crack growth: a comparative study under overload/underload conditions. Theor Appl Fract Mec 2022;118:103268. https://doi.org/10.1016/j.tafmec.2022.103268.
[22] Zhang L, Wei X. Prediction of variable amplitude fatigue crack growth life based on modified grey model. Eng Fail Anal 2022;133:105939. https://doi.org/10.1016/j.engfailanal.2021.105939.
[23] Lam T, Chin H, Zhang X, Feng R, Wang H, Chiang CABB. Tensile overload-induced texture effects on the fatigue resistance of a CoCrFeMnNi high-entropy alloy. Acta Mater 2023;245:118585. https://doi.org/10.1016/j.actamat.2022.118585.
[24] Antunes F-V, Castanheira F-A, Branco R. A numerical analysis of the mechanisms behind plasticity induced crack closure: application to variable amplitude loadings. Int J Fatigue 2016;89:43–52. https://doi.org/10.1016/j.ijfatigue.2015.12.006.
[25] Okorokov V, MacKenzie D, Gorash Y, Morgantini M, van Rijswick R, Comlekci T. High cycle fatigue analysis in the presence of autofrettage compressive residual stress. Fatigue Fract Eng M 2018;41:2305–20. https://doi.org/10.1111/ffe.12866.
[26] He W, Wang C, Deng J, Xie D, Zhang Z. Effect of single overload on fatigue crack growth behavior based on plastically dissipated energy and critical distance theory. Eng Fract Mech 2020;223:106744. https://doi.org/10.1016/j.engfracmech.2019.106744.
[27] Francisco A Díaz G-L, Vasco-Olmo J-M, Antunes F-V, Neto D-M, Díaz F-A. Experimental analysis of the plastic CTOD to characterize the variable amplitude fatigue crack growth in Grade 2 titanium samples. Int J Fatigue 2023;174:107728. Doi: 10.1016/j.ijfatigue.2023.107728.
[28] Cai L, Li W, Hu T, Ji B, Zhang Y, Sakai TABB. In-situ experimental investigation and prediction of fatigue crack growth for aluminum alloys under single spike-overloads. Eng Fract Mech 2022;260:108195. https://doi.org/10.1016/j.engfracmech.2021.108195.
[29] Chen R, Zhu M, Xuan F, Wu S, Fu Y. Near-tip strain evolution and crack closure of growing fatigue crack under a single overload. Int J Fatigue 2020;134:105478. https://doi.org/10.1016/j.ijfatigue.2020.105478.
[30] Geng X, Qin D, Ping Y, Junlin D. Effect of overload on low cycle fatigue crack growth behavior considering accumulative plastic damage. J Fail Anal Prev 2022;22:346–55. https://doi.org/10.1007/s11668-021-01306-4.
[31] Su M, Hu C, Xu L, Feng C, Han Y, Zhao L. Fatigue short crack growth: overload-induced acceleration/retardation behavior. Int J Fatigue 2023;175:107772. https://doi.org/10.1016/j.ijfatigue.2023.107772.
[32] Wheeler O-E. Spectrum loading and crack growth. J Basic Eng 1972;94:181.
[33] Ding Z, Wang X, Gao Z, Bao S. An experimental investigation and prediction of fatigue crack growth under overload/underload in Q345R steel. Int J Fatigue 2017;98:155–66. https://doi.org/10.1016/j.ijfatigue.2017.01.024.
[34] Tu W, Yue J, Xie H, Tang W. Fatigue crack propagation behavior of high-strength steel under variable amplitude loading. Eng Fract Mech 2021;247:107642. https://doi.org/10.1016/j.engfracmech.2021.107642.
[35] Shan J, Wei Z, Xiaoyang L, Fuqiang S. An analytical model for fatigue crack propagation prediction with overload effect. Math Probl Eng 2014;2014:1–9.
[36] Lu Y, Yang F, Chen T. Effect of single overload on fatigue crack growth in QSTE340TM steel and retardation model modification. Eng Fract Mech 2019;212:81–94. https://doi.org/10.1016/j.engfracmech.2019.03.029.
[37] Sun Y, Li X, Yu X, Ge D, Chen J, Chen J. Fracture morphologies of advanced high strength steel during deformation. Acta Metall Sin (Engl Lett) 2014;27:101–6. https://doi.org/10.1007/s40195-014-0032-8.
[38] ASTM E8/E8M. Stand Test Methods for Tensile Testing of Metallic Materials. American Society for Testing and Materials: ASTM; 2013.
[39] ASTM E647. Standard Test Method for Measurement of Fatigue Crack Growth Rates. American Society for Testing and Materials: ASTM; 2015.
[40] Chen C, Ye D, Zhang L, Liu J. DIC-based studies of the overloading effects on the fatigue crack propagation behavior of ti-6Al-4V ELI alloy. Int J Fatigue 2018;112:153–64. https://doi.org/10.1016/j.ijfatigue.2018.03.017.
[41] Casperson M-C, Carroll J-D, Lambros J, Sehitoglu H, Dodds R-H. Investigation of thermal effects on fatigue crack closure using multiscale digital image correlation experiments. Int J Fatigue 2014;61:10–20. https://doi.org/10.1016/j.ijfatigue.2013.11.020.
[42] Wu Y, Bao R. Fatigue crack tip strain evolution and crack growth prediction under single overload in laser melting deposited ti-6.5Al-3.5Mo-1.5Zr-0.3Si titanium alloy. Int J Fatigue 2018;116:462–72. https://doi.org/10.1016/j.ijfatigue.2018.07.011.
[43] Vasco-Olmo J-M, Díaz F-A. Experimental evaluation of the effect of overloads on fatigue crack growth by analysing crack tip displacement fields. Eng Fract Mech 2016;166:82–96. https://doi.org/10.1016/j.engfracmech.2016.08.026.
[44] Vasco-Olmo J-M, Díaz F-A, García-Collado A, Dorado-Vicente R. Experimental evaluation of crack shielding during fatigue crack growth using digital image correlation. Fatigue Fract Eng M 2015;38:223–37. https://doi.org/10.1111/ffe.12136.
[45] Sheu B-C, Song P-S, Hwang S. Shaping exponent in wheeler model under a single overload. Eng Fract Mech 1995;51:135–43. https://doi.org/10.1016/0013-7944(94)00250-L.
[46] Nowell D, de Matos P-F-P. Application of digital image correlation to the investigation of crack closure following overloads. Procedia Eng 2010;2:1035–43. https://doi.org/10.1016/j.proeng.2010.03.112.